Laser Physics and Nonlinear Optics Group (LPNO),
Faculty of Science and Technology & MESA+ Research Institute

University of Twente
Enschede - The Netherlands

Probing the guided modes of a 2D Photonic Crystal Slab using Attenuated Total Reflectance

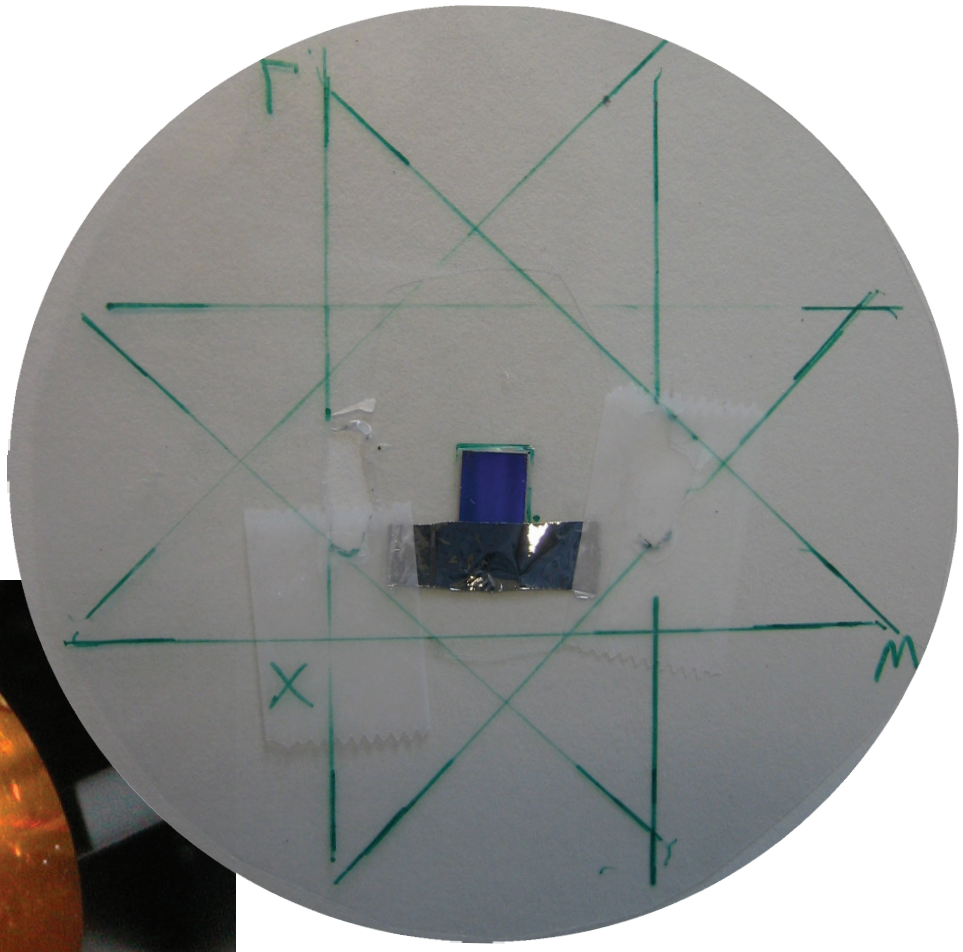

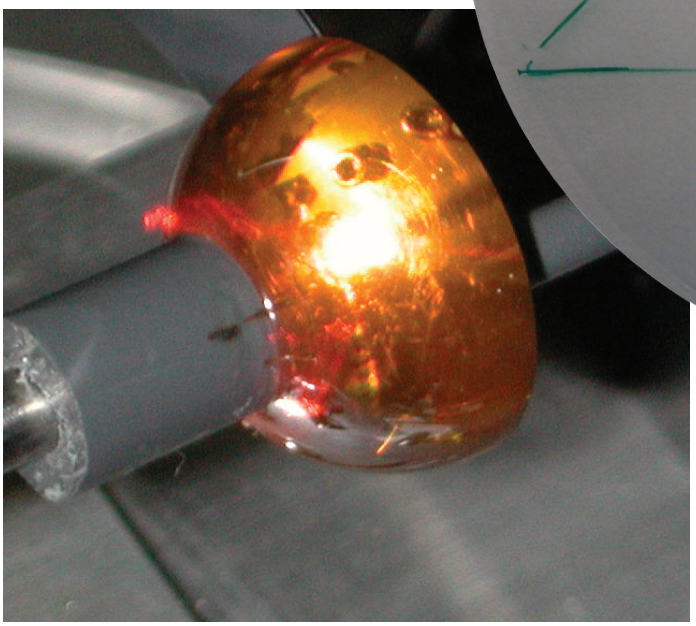

MSc thesis, Roel Arts
Enschede, April 11th, 2008

Probing the guided modes of a 2D Photonic Crystal Slab using Attenuated Total Reflectance

Roel Arts

Graduation Committee:
Prof. Dr. Klaus Boller
Dr. Peter v.d. Slot
Dr. Feridun Ay

University of Twente
Department of Science and Technology
Laser Physics and Nonlinear Optics

Enschede, April 11th, 2008

Abstract

Photonic crystals (PhC) are of special interest in the applications of linear and non-linear optics, as the dispersion of light inside these periodic structures is strongly modified. In this thesis, we present a method to probe the guided modes of a 2D PhC slab that was fabricated for possible non-linear applications. As the guided modes are confined to the PhC slab, a coupling setup had to be devised to access these modes. A coupling setup based on attenuated total reflectance (ATR) was designed and built, and the mid-infrared (MIR) radiation from an optical parametric oscillator (OPO) was used. The measurements performed using this setup are presented and compared to theoretical expectations.

Contents

1. Introduction

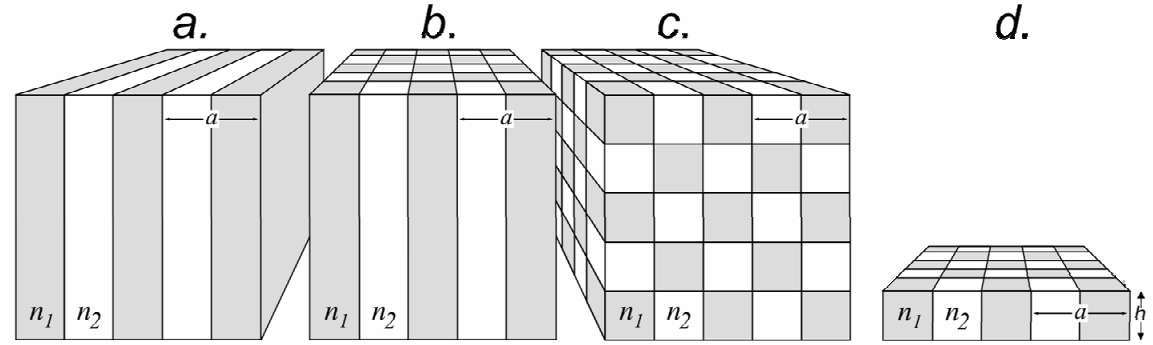

Figure 1.1: Periodic structures in 1, 2 and 3 dimensions and a 2D PhC slab

Photonic crystals (PhCs) are of interest for a multitude of applications. These crystals, which consist of a periodic structure in one, two or three dimensions of materials with different dielectric constants ε, (Fig. 1.1) allow for specifically engineered optical properties. A well-known example of such a structure is the multilayer coating found on mirrors and lenses. These coatings consist of multiple stacked thin layers, usually resulting in either a high reflectivity (HR) or high transmission (AR) for a certain range of frequencies. Other values for the reflectivity are also possible, by choosing appropriate parameters for the layers. These structures have a periodicity of the order of the wavelength of interest, which results in coherent scattering when light propagates through them. This is analogous to the scattering of electrons in a periodic potential, such as that of the atoms in a solid. In the case of a semiconductor, this potential causes a band gap to open up between the valence and conduction energy bands. Electron states with energy levels lying inside this band gap are not allowed. Similarly, in a periodic dielectric structure, scattering of the waves at the interfaces between the different dielectrics modifies the optical bands, i.e., the waves with frequencies ω_n that can propagate with a certain wave vector $\vec{k}$ are modified. In some cases, a band gap opens up. Optical frequencies that are inside this photonic band gap (PBG) are forbidden to be generated or to propagate inside the crystal. More specifically, there is no real value of $\vec{k}$ for which a frequency ω_n can be found that is inside this PBG. Because this optical band structure of allowed and forbidden photon energy (frequency) states is similar to the electron energy bands inside a semiconductor, these structures are called Photonic Crystals.

For a true photonic band gap, where no propagation is allowed for any direction and polarization within a certain frequency band, a three-dimensional structure is required (3D PhC [1, 2, 3]). However, photonic effects can also be applied in one or two dimensions. A 1D example of this is the aforementioned high-reflectivity coating on mirrors. One could say that because of the PBG, a certain frequency range of incident radiation is forbidden to propagate through the coating and is therefore completely reflected.

The PBG makes spectral filtering of light one obvious application of PhC's. Confinement of light is another. For example, by placing a photonic structure around a waveguide channel, light which has a frequency inside the PBG can be prevented from leaving the waveguide.

A large variety of photonic crystal designs can be imagined. Of special interest are two-dimensional slab structures, because they are relatively easy to fabricate compared to PhCs with a full three-dimensional periodicity. These typically consist of a periodic pattern of air holes in a film of high-index material. The thickness of the film (*h* in Fig. 1.1d) is typically in the order of the wavelength for which the PhC was designed. Such crystals are called two-dimensional photonic crystal slabs (PhC slabs). Because the refractive index of the slab material is much larger than that of the surrounding material, e.g. air, index guiding can occur. This is analogous to the guiding of light inside a planar (slab) waveguide, where modes with a sufficiently high in-plane wave vector $\vec{k}_{\parallel}$ are confined to the slab. These modes have a concentration of their field energy inside the waveguide slab, with an evanescent tail extending outside of it.

Although a two-dimensional periodic crystal (Fig. 1.1b) can never have a PBG in all three dimensions, a 2D PhC slab (Fig. 1.1d) can have a complete PBG for modes that are confined to the plane of the slab by index guiding, named "guided modes". Although the confinement of the guided modes allows for a strong enhancement of the intensity in the slab as well as numerous other advantages, the confinement makes it difficult to couple light from an external source into these guided modes. Photonic properties are also evident in modes not confined to the slab (called "leaky modes" [2]), but these modes are not at the focus of this thesis. As the leaky modes of 2D PhC slabs have been studied elsewhere, also by us [10-12], they will not be discussed any further here.

Until now, we have discussed the linear properties of PhCs. Even more interesting effects can be found by making use of materials with a non-linear ($\chi^{(3)}$) optical response, for example materials strongly exhibiting the Kerr effect [4]. Since the frequency range covered by the PBG depends on the dielectric constants of the materials the PhC is composed of, the Kerr effect can be used to rapidly "switch" the position of the PBG [5], thereby enabling rapid switching of light within a certain frequency range.

To study the combination of photonic and non-linear effects, a 2D PhC slab sample was fabricated with the goal to demonstrate rapid (fs) all-optical switching in a subsequent experiment. Silicon was selected because it is a high-index material, it has a $\chi^{(3)}$ nonlinearity higher than that of other materials (e.g., glass) and it can be easily processed with the available infrastructure. Furthermore, its thermal conductivity and high optical damage threshold [6] mean that higher intensities of incident light can be used to generate a measurable Kerr-effect. The electronic band gap of crystalline silicon at room temperature is about 1.11 eV. This means that for wavelengths longer than 2.25 µm, two-photon absorption is suppressed, which would otherwise slow down the third-order response, thus limiting the speed of optical switching [7]. Therefore, a lattice design was chosen with a PBG around 2.5 µm, which corresponds to photon energies that are too low for two-photon absorption. The chosen design corresponds to a 2D square lattice of 1 µm spaced air holes in a 500 nm thick Si layer. A Silicon-on-Insulator slab geometry was chosen as a practical implemetation of this design. In this geometry, the photonic slab is supported by a layer of low-index material (in our case, SiO_2 on top of a Si bulk wafer) to enable the fabrication of a more robust, large-area sample.

To achieve field localization required for enhanced non-linear effects, the guided modes of the crystal need to be used. The reason is that these modes are confined to the PhC slab, such that the light intensity will be enhanced inside the crystal, which corresponds to a longer effective interaction length in the silicon. However, index guiding makes these modes difficult to access, as free-space waves can never have a wave vector k large enough to couple to the sample's guided modes.

The main goal of this research project was to probe the guided modes of our 2D PhC sample. Several alternative methods were examined for this. As stated earlier, guided modes have an evanescent tail outside the waveguiding layer. This evanescent field is accessible and can be used to probe the guided modes. In this thesis, we have chosen to use attenuated total reflection inside a high-index material, where coupling to the guided modes in the PhC is obtained through the evanescent field associated with the total internal reflection within a high-index material.

To probe the guided modes around 2.5 μm we have chosen to use an optical parametric oscillator (OPO). The OPO is capable of generating mid-infrared (MIR) waves with vacuum wavelengths between 2.6 and 4 μm, enabling the probing of modes with photon energies around and below the envisioned PBG. The band just below the PBG is of special interest for nonlinear applications, as for these modes, due to a reduced group velocity, the electric field energy is expected to concentrate inside the silicon slab, leading to possible enhancement of nonlinear effects.
The reason to use an OPO instead of seemingly simpler alternatives, such as using spectrally-filtered output from a white light source, is that the OPO is superior in terms of high output power in a narrow spectral bandwidth in a high-quality (diffraction-limited, laser-like) beam. Since the OPO produces a single spatial mode, the numerical aperture of the reflection inside the high-index medium can be kept low, leading to a better resolution with which $\vec{k}_{\parallel}$ can be set. The narrow spectral bandwidth allows a spectral resolution much better than is needed to identify photonic resonances.

The remaining part of this thesis is structured as follows: we will start by recalling the theory used to describe the properties of a PhC in chapter 2. This chapter will also present some details on the expected theoretical properties of the particular PhC samples that are investigated here. After that, we will discuss a number of guided-mode coupling alternatives as well as the principles of evanescent field coupling (chapter 3). Some design choices of our ATR coupling setup will also be briefly discussed. Chapter 4 presents a number of experimental aspects, starting with sample design and fabrication, followed by a description of the MIR radiation source that was used and ending with an overview of the experimental setup. Chapter 5 presents the results obtained with this setup. Finally, some conclusions and recommendations will be presented (chapter 6).

2. Photonic crystals

Photonic crystals (PhC) are structures with a periodically-varied dielectric constant ε. This periodic variation is typically accomplished by alternating between two different materials along one or more dimensions in space. In this chapter, we give a short overview by recalling the theory of photonic crystals as applied to the specific case of our sample. We will start with the illustrative example of a multilayer mirror, which can be seen as a photonic crystal in one dimension. This example will first be discussed qualitatively, after which the Maxwell equations will be investigated for this arrangement. After that, we will extend the Bragg mirror model to the case of a two-dimensional PhC slab. A further discussion will be presented on the mechanism of index guiding and field confinement, which is important when applying this theory to photonic crystal slabs. Once the geometric properties of photonic crystal slabs and the theory behind their optical response are understood, a numerical method for computing the band diagram will be briefly discussed. Finally, the sample used in our experiments will be briefly discussed and some simulations regarding its properties will be presented. As the more specific sample design considerations and material choices have little direct relevance there, these will be discussed later, in section 4.1.

2.1 The Bragg mirror and the Bloch theorem

A multilayer stack or "Bragg mirror" is the simplest example of a photonic crystal and it is therefore a mathematically-simple, illustrative example to explain the physical origin of a PhC's optical properties.

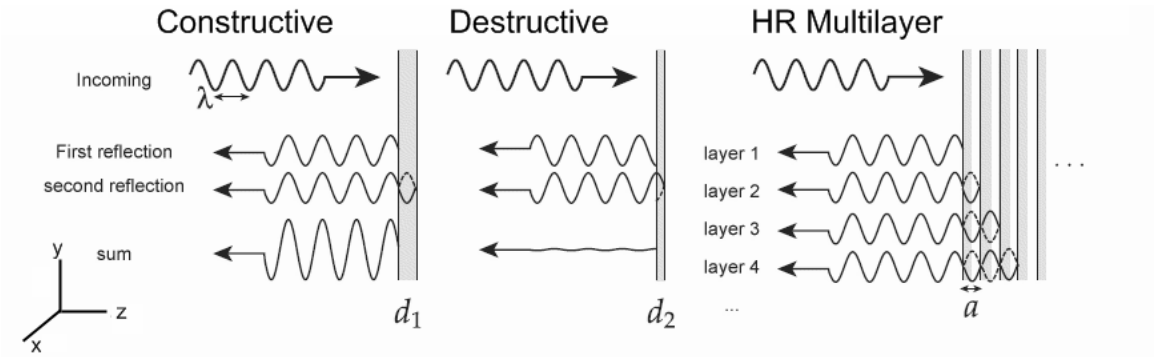

Figure 2.1: The Bragg mirror

A Bragg mirror, as can be seen in Fig. 2.1, consists of alternating layers with usually two different dielectric constants, ε_1 and ε_2, and with thicknesses d_1 and d_2, respectively. The structure therefore has a spatial periodicity $a = d_1 + d_2$ in the dielectric constant. It is this spatial periodicity that gives these mirrors a reflectivity that is highly dependent on the frequency of light incident on the surface, allowing them to be used e.g. to filter or reflect certain desired frequencies.
This effect can be intuitively explained by interference effects (Fig. 2.1). If the reflected waves from each interface between the two materials interfere constructively, the stack is highly reflective; if they interfere destructively, the stack is highly transmitting.

The starting point for mathematical treatment of this and related optical phenomena are the macroscopic Maxwell equations, given in Eqs. 2.1. [4]

$$\begin{aligned} \nabla \cdot \vec{B} &= 0 & \nabla \times \vec{H} - \frac{\partial \vec{D}}{\partial t} &= \vec{J} \\ \nabla \cdot \vec{D} &= \rho & \nabla \times \vec{E} + \frac{\partial \vec{B}}{\partial t} &= 0 \end{aligned} \tag{2.1}$$

For a dispersion-free, lossless isotropic medium the dielectric displacement $\vec{D}$ is related to the electric field $\vec{E}$ by the relative dielectric permittivity ε. Furthermore, we restrict this discussion to materials where the relative magnetic permeability $\mu = 1$, so that $\vec{B}$ is related to $\vec{H}$ by the vacuum permeability:

$$\vec{D} = \varepsilon_0 \varepsilon \vec{E} \qquad \vec{B} = \mu_0 \vec{H} \tag{2.2}$$

Another assumption that we will make here is that there is no free current or free charge inside the material, meaning that both $\vec{J}$ and ρ are zero. These assumptions are well fulfilled in most dielectric materials.

Finally, we regard ε as being scalar (isotropic materials), non-dispersive (no frequency dependence) and purely dependent on position $\vec{r}$, while $\vec{H}$ and $\vec{E}$ remain dependent on both time t and position $\vec{r}$. These approximations allow Eqs. 2.1 to be reduced to the following set of equations:

$$\begin{aligned} \nabla \cdot \vec{H}(\vec{r},t) &= 0 & \nabla \times \vec{H}(\vec{r},t) - \varepsilon_0 \varepsilon(\vec{r}) \frac{\partial \vec{E}(\vec{r},t)}{\partial t} &= 0 \\ \nabla \cdot [\varepsilon(r) \vec{E}(\vec{r},t)] &= 0 & \nabla \times \vec{E}(\vec{r},t) + \mu_0 \frac{\partial \vec{H}(\vec{r},t)}{\partial t} &= 0 \end{aligned} \tag{2.3}$$

The linearity of Eqs. 2.3 means that any solution of Eqs. 2.3 can be expressed as the sum of harmonic modes. The most important property of these harmonic modes is that the time- and space-dependence of the H- and E-fields can be factorized:

$$\vec{H}(\vec{r},t) = \vec{H}(\vec{r}) e^{-i\omega t} \qquad \vec{E}(\vec{r},t) = \vec{E}(\vec{r}) e^{-i\omega t} \tag{2.4}$$

We can now eliminate either $\vec{H}(\vec{r})$ or $\vec{E}(\vec{r})$ from Eq. 2.3. For mathematical convenience, we choose to retain $\vec{H}(\vec{r})$, as follows:

$$\nabla \times \left(\frac{1}{\varepsilon(\vec{r})} \nabla \times \vec{H}(\vec{r}) \right) = \left(\frac{\omega}{c} \right)^2 \vec{H}(\vec{r}) \tag{2.5}$$

Eq. 2.5 has the mathematically-convenient form of an eigenvalue problem, where $c = \frac{1}{\sqrt{\mu_0 \varepsilon_0}}$ is the speed of light in vacuum.

The divergence equations in Eqs. 2.3 are automatically fulfilled if we assume that solutions of $\vec{E}(\vec{r})$ and $\vec{H}(\vec{r})$ are transversal waves and that there are no point sources or sinks inside the material.

In the case of a uniform medium, in which $\varepsilon(\vec{r}) = \varepsilon$ for all $\vec{r}$, solutions of Eq. 2.5 take the form:

$$\vec{H}_k(\vec{r}) = \vec{H}_0 e^{-i\vec{k} \cdot \vec{r}} \tag{2.6}$$

These solutions are plane waves, with the transversality requirement:

$$\vec{H}_0 \cdot \vec{k} = 0 \tag{2.7}$$

By inserting these solutions into Eq. 2.5, we obtain the dispersion relation, relating wave vectors $\vec{k}$ to eigenvalues, or frequencies ω:

$$\omega = \frac{|\vec{k}|c}{\sqrt{\varepsilon}} \tag{2.8}$$

The next step in our analysis consists of solving Eq. 2.6 for a periodic medium, in this case a Bragg mirror. Even though this problem can also be solved using a scalar representation of the spatial coordinate and the field, we will use vector notation as this representation can be easily extended to more dimensions.
As can be seen in Fig. 2.1, the dielectric constant varies periodically along the z-axis. This can be expressed as:

$$\varepsilon(\vec{r}) = \varepsilon(\vec{r} + \vec{a}) \qquad \vec{a} = a\hat{z} \tag{2.9}$$

Here, $\vec{a}$ is called the real-space lattice vector for this structure, as it contains information on the real-space periodicity of the structure, and $\hat{z}$ is a unit vector in the positive z-direction. The structure can be completely defined by defining a primitive unit cell. In the case of a Bragg mirror, the unit cell consists of a layer with thickness d_1 and dielectric constant ε_1 on top of a layer with thickness d_2 and dielectric constant ε_2.
In general, it is useful to look for additional symmetries in the unit cell. In this particular case, no additional structural symmetries can be found.

For a further simplification, the Bloch theorem can be applied [8]. It states that solutions of Eq. 2.5 must be of the form:

$$\vec{H}(..., z) \propto e^{ik_z z} \cdot \vec{u}_{k_z}(..., z) \tag{2.10}$$

These solutions are called Bloch modes, which can be regarded as plane waves modulated by a spatially-periodic function $\vec{u}_{k_z}$ with the same period as the lattice. For the media under consideration the Maxwell equations are time-symmetric, meaning that if a forward-propagating solution exists, this solution also exists as a backward-propagating wave:

$$\omega_n(\vec{k}) = \omega_n(-\vec{k}) \tag{2.11}$$

Bloch modes are periodic in k_z with the period a of the lattice, which means that:

$$\omega_n(k_z) = \omega_n(k_z + \frac{2\pi}{a}) \tag{2.12}$$

At this point, it is convenient to introduce a so-called reciprocal lattice vector $\vec{G}$, which contains the same information as the vector $\vec{a}$:

$$\vec{G} = \frac{2\pi}{a}\vec{z} \tag{2.13}$$

The reciprocal lattice vector allows for a discussion of lattice geometry in wave vector space. Similarly, a primitive unit cell can be defined in wave vector space, called the Brillouin zone. It is defined as the area spanned by the reciprocal lattice vectors. Eq. 2.12 states that the dispersive properties of the structure can be completely defined by calculating $\omega_n(k_z)$ for values of k_z in the Brillouin zone. Furthermore, Eq. 2.11 states that half the Brillouin zone already contains the full information about the dispersion within the multilayer mirror. This half is called the irreducible Brillouin zone (iBZ). This concept, and the role of symmetry in defining the iBZ, will be discussed in more detail in the next section.

The dispersion of the structure can now be plotted in a so-called band diagram, where the frequencies ω_n of solutions to Eq. 2.5, normalized to $2\pi/a$, are plotted against the associated wave vector k_z in the direction of periodicity. Such a band diagram, for a structure with $\varepsilon_1 = 13$, $d_1 = 0.2a$, $\varepsilon_2 = 1$ and $d_2 = 0.8a$ is shown in Fig. 2.2 [2]:

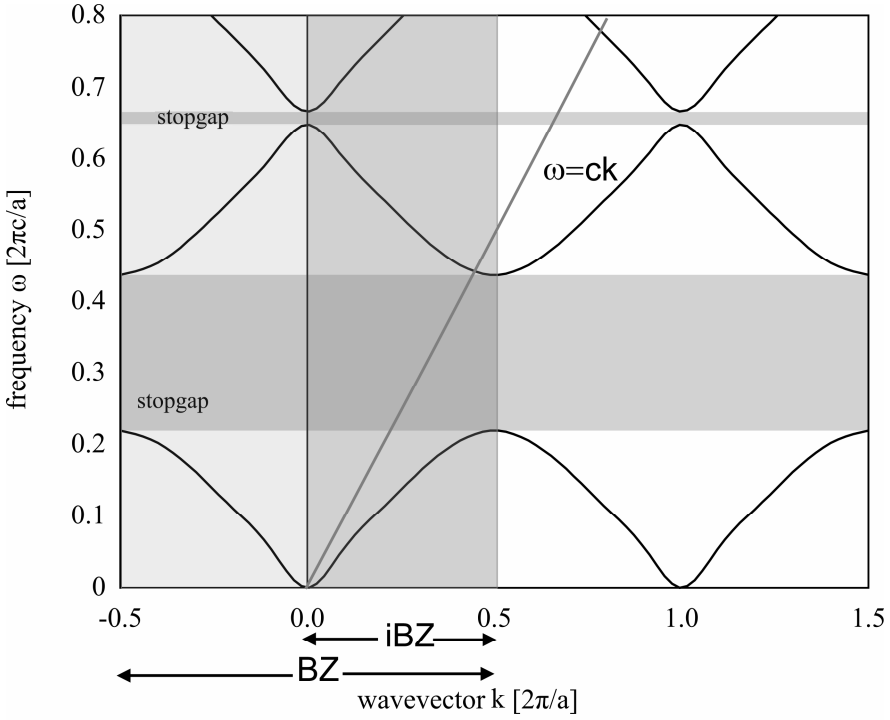

Figure 2.2: Band diagram of a 1D PhC, taken from [2]

As can be seen in Fig. 2.2, no solutions $\omega_n(k_z)$ exist for certain frequency ranges. These ranges are called stop gaps. It should be noted that the band diagram shown is expected only for an infinite periodic structure with an infinite number of layers. In reality, a Bragg mirror is finite, leading to smaller stop gaps. Because no propagating modes are present for frequencies inside this stop gap, a Bragg mirror is highly reflective for these frequencies. Fig. 2.2 also shows the so-called vacuum light line, $\omega = ck$. For normal incidence in vacuum, the intersection points between this light line and the bands give the frequencies for which the mirror is highly transmitting, as the incident light can excite propagating modes inside the multilayer structure.
The periodicity of the band structure as expressed in Eq. 2.11 and 2.12 is apparent in this figure. This repetition of the band structure is also referred to as “folding”. Now that the 1D example has been discussed, we will extend this theory to the two-dimensional case, which is of higher interest in this thesis.

2.2 Bloch modes in more dimensions and exploiting symmetry

The solution of the wave equation (Eq. 2.10) can be generalized to more dimensions in space. For example, if the structure is periodic in three dimensions, three linearly independent lattice vectors can be defined with which the periodicity of the crystal can be described. For all of these vectors $\vec{a}_n$, Eq. 2.9 holds true; similarly, the periodic envelope $\vec{u}_k$ in Eq. 2.10 must now be invariant over addition of arbitrary combinations of these lattice vectors. The consequence of Bloch’s theorem is then

that allowed modes with the dispersion $\omega_n(k)$ must also be invariant through addition of reciprocal lattice vectors. Let us now regard the specific case of a two-dimensional square lattice of holes in a high-index material, as shown in Fig. 2.3, because a crystal of this type is investigated in this thesis.

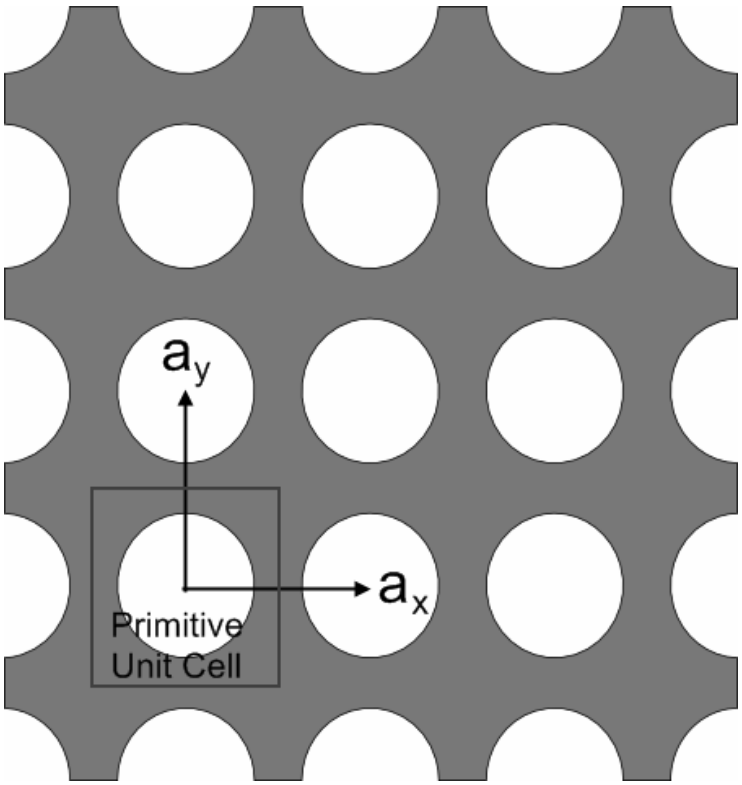

Figure 2.3: a square lattice of air holes in a high-index material

This lattice can be completely characterized by its primitive unit cell and the vectors under which the unit cell needs to be translated in order to construct the entire lattice. The primitive cell in real space is given by a single square with a single air hole in it. In order to construct the entire lattice from this primitive cell, multiple sets of lattice vectors can be defined. An obvious choice in the example above would be $\vec{a}_1 = \vec{a}_x = a\hat{x}$ and $\vec{a}_2 = \vec{a}_y = a\hat{y}$. We use these vectors to obtain the first Brillouin zone, which constitutes the primitive cell in reciprocal space.

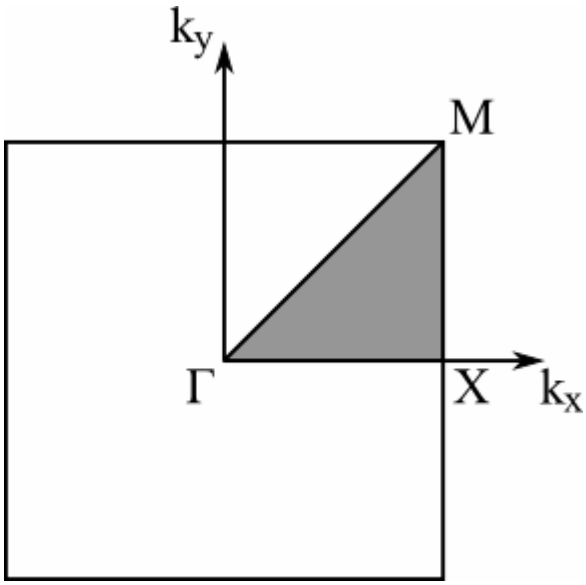

Figure 2.4: The first Brillouin zone and the irreducible Brillouin zone

At this point, it is convenient to look for further symmetries for further simplification. Since the lattice is square, it is invariant to translation along the lattice vectors by an integer multiple of these vectors, but it is also invariant to rotations by 90 degrees. This means that if one calculates the modes $\omega_n(k_{\parallel,1})$ belonging to a certain in-plane wave vector $k_{\parallel,1}$, then using an in-plane wave vector $k_{\parallel,2}$, which is $k_{\parallel,1}$ rotated over an angle of 90°, will yield the same modes: $\omega_n(k_{\parallel,1}) = \omega_n(k_{\parallel,2})$.

In addition, the time-reversal symmetry mentioned in Eq. 2.11 holds true. If all these symmetry arguments are applied to the Brillouin zone, one can minimize the wave vector space that still contains the full information about the crystal's optical properties. In other words, if one obtains the band structure $\omega_n(k_\parallel)$ for all $k_\parallel$ within this area, one can also obtain $\omega_n(k_\parallel)$ for k outside of these area by applying the appropriate transformations, which in this case are: rotations by 90°, time-reversal (Eq. 2.11) and addition of integer multiples of reciprocal lattice vectors.

The minimum area in wave vector space from which, in this manner, the optical properties of the structure can be derived for the entire wave vector space, is called the irreducible Brillouin zone (iBZ) and is indicated in Fig. 2.4 by the grey shaded area. Within this zone, a number of high-symmetry points can be defined. These points lie on the corners of the iBZ and are by convention labeled as Γ=(0,0), X=($\frac{2\pi}{a_x}$,0) and M=($\frac{2\pi}{a_x}$,$\frac{2\pi}{a_y}$). These points are used to name unique propagation directions inside the crystal. Γ-X and Γ-M are two of those directions, as are all the vectors obtained by rotating Γ-X to Γ-M. All other vectors inside the crystal yield identical mode structures due to the aforementioned crystal symmetries. For instance, wave vectors along the X-M direction correspond to those lying along the Γ-X direction, due to the structure's 90° rotational symmetry.

With the 1D example, we have implicitly assumed the wave vector to point in the direction of the crystal's periodicity. Due to homogeneity in the transversal plane, a distinction between TE and TM polarized fields did not need to be made. However, in

the case of 2D structures, the transversal plane is no longer homogeneous, and TE and TM polarizations each have different solutions to Eq. 2.5.
It is also important to note that a 2D PhC does not confine light in the third dimension. Therefore, 2D photonic structures are typically fabricated in a thin-film (slab) planar waveguide, where the light is confined in the third dimension by index guiding. Before calculating the band structure for the PhC under investigation, we will discuss this index guiding mechanism that confines Bloch modes to the plane of the photonic slab. We will then return to the theory with a short discussion of the numerical algorithm used to compute the band diagram that is associated with a 2D PhC slab.

2.3 Index guiding and the light line

As stated before, a two-dimensional photonic crystal cannot provide full control over light in three dimensions. Therefore, a principle called index guiding is used to confine light to a planar waveguide. This principle is related to total reflection at an interface, which is shown in Fig. 2.5.

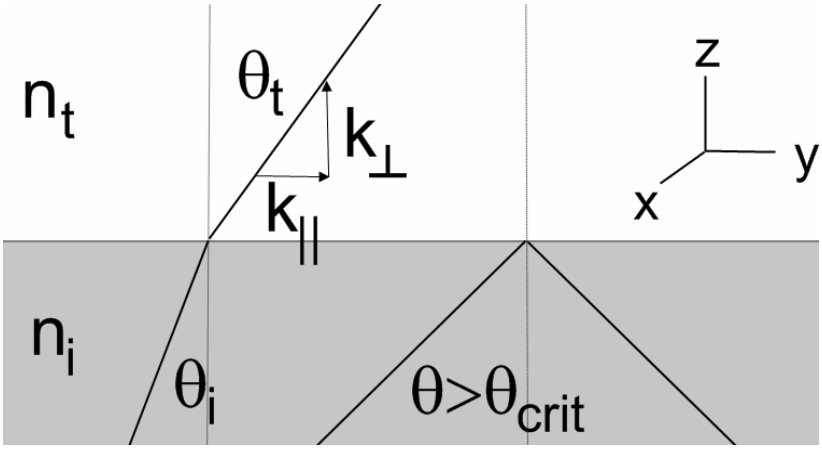

Figure 2.5: Total internal reflection

The waveguiding mechanism can be qualitatively understood using Snell's law [4] for refraction at an interface between two dielectrics, which states that:

$$n_i \sin\theta_i = n_t \sin\theta_t \tag{2.14}$$

If $n_t < n_i$, for a certain angle θ_{crit}, $n_i \sin\theta_{crit} = n_t$. Therefore, for incident angles internal to the slab $\theta_i > \theta_{crit}$, no solution to Eq. 2.14 exists. This means that incident light is totally reflected beyond this angle. This is called total internal reflection (TIR).
In the case of thin layers, this picture is actually oversimplified because ray optics can no longer be used. A more appropriate picture of wave propagation in thin layers is to state this in terms of conservation of energy as well as conservation of momentum. Energy conservation in this case merely means that the light frequency ω is preserved. As both dielectrics are invariant under translation along the interface, the wave vector component parallel to the interface, $k_{\|}$, is also a conserved quantity. To describe the consequences of this, let us take an arbitrary parallel wave vector component $k_{\|}$ in the high-index slab. For this wave vector to be able to couple to the low-index material, the following equation needs to hold:

$$\omega = \frac{c}{n_i}\left|\vec{k}_i\right| = \frac{c}{n_i}\sqrt{k_{\parallel}{}^2 + k_{\perp,i}{}^2} = \frac{c}{n_t}\left|\vec{k}_t\right| = \frac{c}{n_t}\sqrt{k_{\parallel}{}^2 + k_{\perp,t}{}^2} \tag{2.15}$$

To describe the typical situation of a slab suspended in air, we now assume, without loss of generality, that $n_t = 1$, which means that $\left|\vec{k}_t\right| = \frac{\omega}{c}$. Since $n_i > n_t$, we can now choose $k_{\parallel} > \left|k_t\right|$. This represents a wave propagating inside the high-index material without damping. As a result, in order for Eq. 2.15 to hold, $k_{\perp,t}{}^2 < 0$. This means that $k_{\perp,t}$ is now imaginary, representing a wave that is damped upon propagation. This imaginary wave vector component no longer represents a propagating wave. Instead, the wave is evanescent in the low-index material and energy no longer propagates into this material. This is true in the case of a PhC slab as well. As can be seen in section 2.5, the PhC modes lying below the so-called "light line" have a $k_{\parallel}$ that is too large to couple to a propagating free-space beam; hence, these modes are evanescent outside of the PhC slab. The condition for which there no longer is a propagating wave with a real-valued $k_{\perp,t}$ in Eq. 2.15 corresponds to the condition for total internal reflection in Eq. 2.14. The imaginary $k_{\perp,t}$ also tells us that total internal reflection is always accompanied by an evanescent wave in the low index material.
Using this principle of total reflection, generally referred to as "index guiding", one can confine the propagation of light to, for instance, the in-plane direction of a slab. Slab modes that are confined in this manner are referred to as guided modes. Although propagation of these modes is confined to the slab region, one can still couple to these guided modes through the evanescent wave, as will be shown below.

Equation 2.15 will be important later on, when discussing coupling to guided modes (see section 3.1.3). It is important to note that for a slab, modes can no longer be classified as purely TE or TM, as a slab does not show a continuous translational symmetry in the direction normal to the slab. However, in the special case where the top and bottom cladding layers have the same refractive index, there is a mirror symmetry with regard to the z=0 plane and modes can be classified as either having "even" or "odd" symmetry, as shown in Fig. 2.6. The properties of the evanescent field will be discussed in more detail in chapter 3.

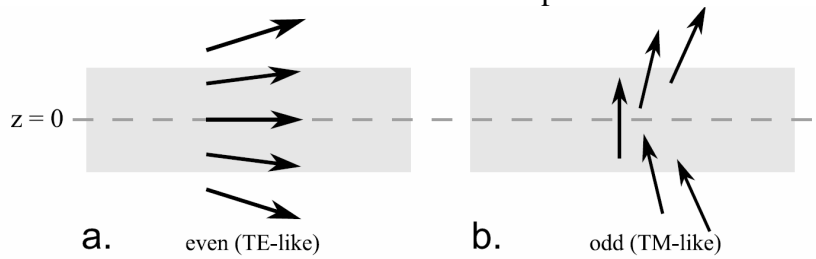

Figure 2.6: Axis of the E-field with even (left) vs odd (right) mode symmetry

In the general case of an index difference between the cladding layers, symmetry is broken and there will be a weak coupling between even-like and odd-like modes.

2.4 MPB: Eigenstates using a frequency-domain method in a plane-wave basis

Several numerical methods are available for computing the optical properties of a PhC. As our research focuses on the use of guided modes, we will only examine the

method most suitable for the calculation of those. As stated earlier, a guided mode can be viewed as the product of a periodic field distribution and a plane wave. Since the field distribution envelope is periodic, one can apply Fourier theory and express $\vec{u}_k$ as the sum of discrete spatial frequency components; in other words, spatial harmonics of the lattice itself. While computing the exact Bloch envelope $\vec{u}_k$ as the sum of plane waves would require an infinite basis of plane waves, accuracy can be maintained by choosing a sufficiently large basis; $N >> n$, where N is the number of basis vectors and n is the number of bands that are computed. [9]
It should be noted that for accurately calculating the band diagram of a PhC slab, a full 3D calculation is necessary. As the 3D plane-wave Fourier method discussed in this section assumes periodic boundary conditions, this means that the calculation also assumes a periodicity in the direction normal to the slab – in other words, the PhC slab is repeated infinitely in the calculation. This has the consequence that only the modes below the light line, which are confined to the slab, are calculated accurately.

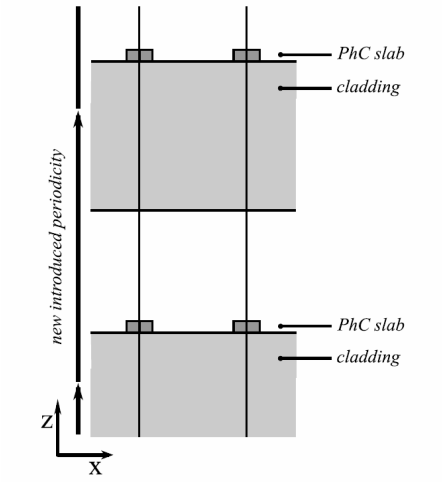

Figure 2.7: MPB supercell with additional z-periodicity

The theoretical band diagrams presented in this thesis were calculated using the MIT Photonic Bands (MPB) package [9], which implements an eigensolver for an arbitrary periodic dielectric structure using the numerical methods described above. The band diagrams calculated by this package are presented in section 2.5.

2.5 The band diagram and previous characterization

The leaky modes of the PhC sample that is under investigation here have previously been characterized by specular reflectance [10, 11] and transmission [11, 12] measurements. Rigorous Coupled Wave Analysis (RCWA) calculations [11, 12, 34] were fitted to the experimental data from these experiments. For our own calculation of the band structure of the guided modes, we have used the parameters resulting from this fit. The consistence of the named experimental data with the model prediction suggests that these parameters provide a suitably accurate description of the structure. Table 2.1 shows these parameters used for the band diagram calculation compared to the design parameters applied to crystal fabrication [13], discussed in more detail in section 4.1. This table shows that the fit parameters used for the band diagram calculations closely match the original fabrication goal.

Table 2.1: MPB parameters vs. fabrication parameters

	RCWA fit / MPB simulation	LIL fabrication goal
Slab height h (µm)	0.55	~ 0.5
Hole radius r (µm)	0.38	~ 0.40
Lattice period a (µm)	1.00	1.00
Relative permittivity ε_{Si}	11.9	11.9

As stated in section 2.3, the guided modes of a finite-height slab structure do not exhibit a pure TM or TE polarization. Furthermore, a slab structure with asymmetric cladding (such as the PhC investigated here) does not exhibit modes that can be classified as purely "even" or "odd", either. Correspondingly, in order to obtain an accurate theoretical band diagram, no assumptions on field distribution symmetry were made. However, in order to predict whether specific modes can be excited by incident TE or TM polarized light, the theoretical band diagram was compared to band diagram calculations in which the cladding was assumed symmetric (Fig. 2.8b). A vertical slice of the MPB unit cells used in these simulations can be seen in Fig. 2.8. The four lowest bands in the band diagram (Fig. 2.9) were classified according to similarity to even and odd modes found using the unit cell from Fig. 2.8b (band diagram in Fig. 2.10). For clarity, only bands within the examined spectral range (see chapters 4 and 5) are shown. The high degree of similarity between the dispersion in Figs. 2.9 and 2.10 suggests that, e.g., bands labeled as even-like in Fig. 2.9 can be excited with linearly polarized light. This comparison was validated by comparing the field distribution output from MPB for both structures. No clear field distribution symmetry could be found for the fifth band in Fig. 2.9.
The gray region in Fig. 2.9 and 2.10 indicate the light cone, bounded by the light line. Modes lying in in light cone can couple directly to free space radiation, as discussed in section 2.3.

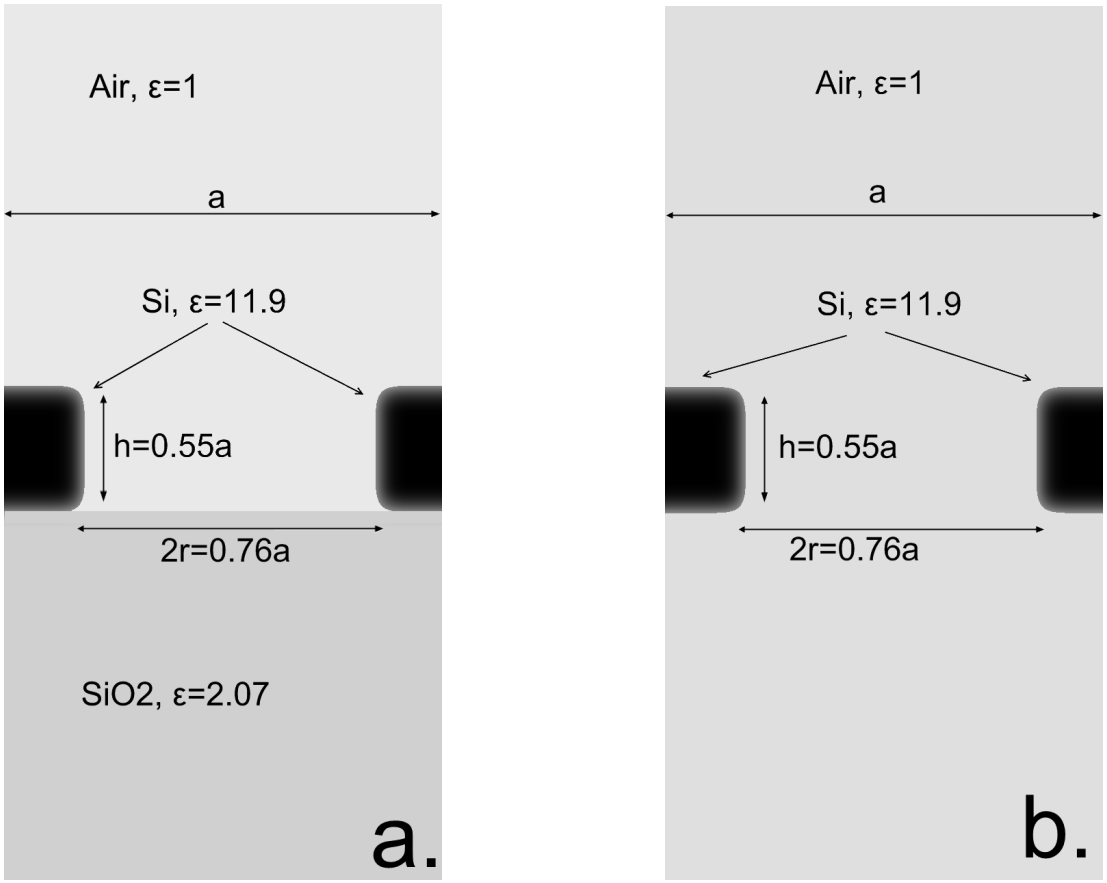

Figure 2.8: MPB computation cells. Left (a): asymmetric cladding, right (b): symmetric cladding

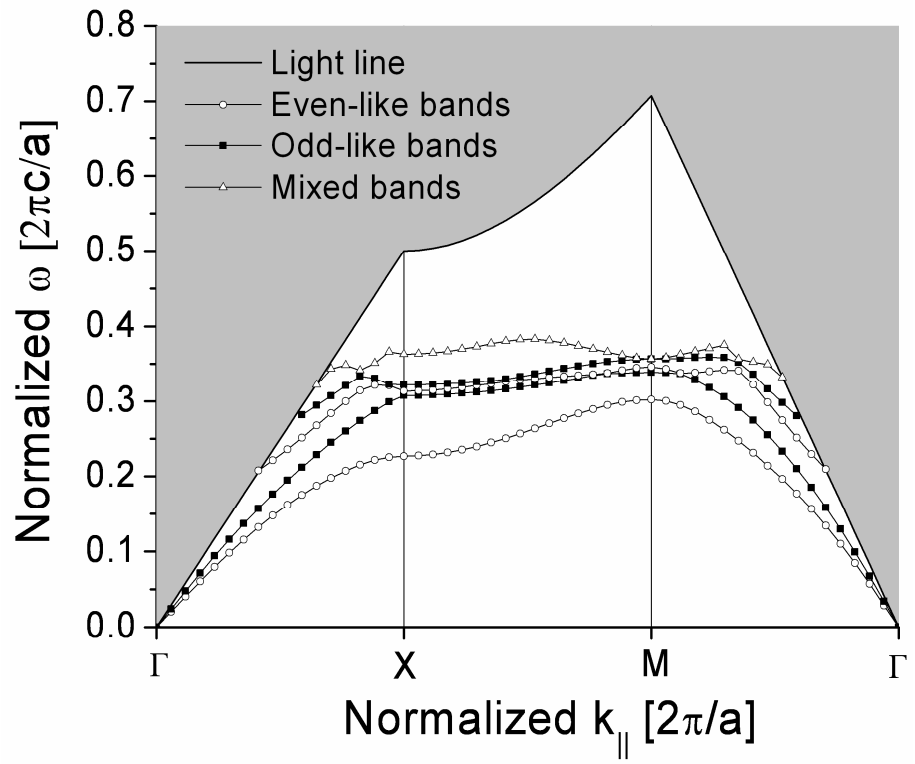

Figure 2.9: Band diagram calculation - asymmetric cladding (see Fig 2.8a)

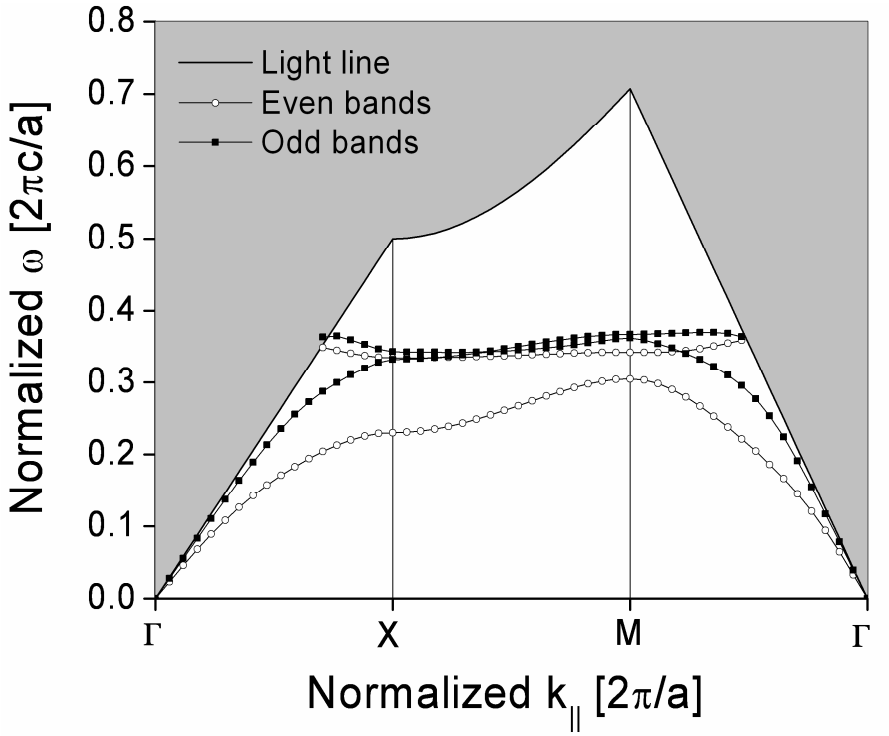

Figure 2.10: Band diagram calculation - symmetric cladding (see Fig 2.8b)

3. Evanescent field coupling

This chapter discusses the method that was chosen for probing the guided modes of our 2D PhC slab. Some alternatives will be discussed and the choice for evanescent-field coupling will be motivated. After that, the theoretical properties of the evanescent field will be discussed. Thereafter we present the chosen coupling geometry and discuss the parameters which determine the coupling efficiency. We continue with a discussion of a distance control scheme, which is of critical importance to obtaining reliable measurements. Since this distance control scheme depends on a bending deformation of the sample, a simulation of this deformation will be presented as well.

3.1 Coupling to guided modes

As was discussed in chapter 2, free-space radiation is never phase-matched to a guided mode, i.e. the wave vector of incident radiation cannot be made equal to the wave vector of a guided mode at any angle of incidence and at any frequency. Therefore, an incident out-of-plane free-space beam can never couple to a guided mode. However, the properties of the guided modes can be probed by perturbing the modes sufficiently to couple light from an external source into the structure. Various methods are known to accomplish this. In order to select the best alternative, we recall that the goal of this project is to probe the guided modes, thereby obtaining experimental data to construct (part of) an accurate band diagram. In other words, one needs to measure $\omega(k)$; therefore, knowledge of both ω and k of the mode in which coupling was achieved is required. The criterion by which we will evaluate the coupling alternatives is mode-specific coupling.

3.1.1 End-fire coupling

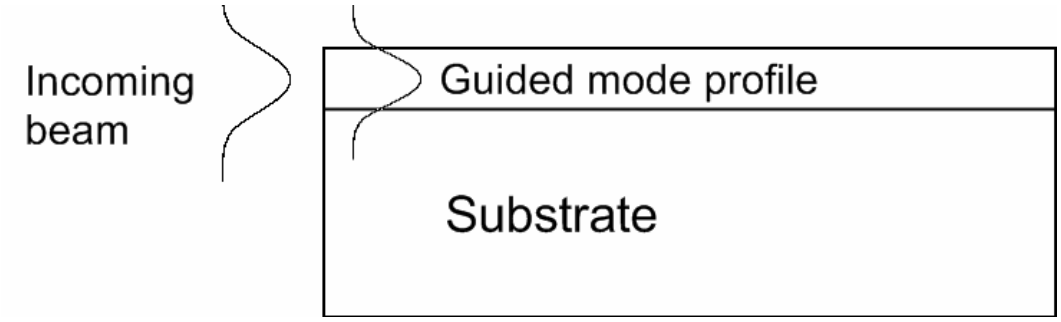

Figure 3.1: End-fire coupling

The most obvious way to couple light into a guided mode is to focus a beam onto an end face of the crystal slab (see Fig. 3.1). The amount of power transferred into a guided mode then depends on the degree of similarity between the incoming beam's field profile and the field profile of the light diffracted out of a particular guided mode. However, in the case of the PhC slab under investigation, this would result in a poor transfer of power. The reason for this is that our photonic layer is only 0.5 µm thick and the spectral range of interest encompasses vacuum wavelengths of 3 µm.

With these parameters, simply focusing an incoming beam in air would result in a spot size much larger than the crystal thickness.
This problem could potentially be overcome by constructing a "taper" structure, where the field profile is adiabatically changed to match that of the PhC guided mode. For our purposes, however, this method is unusable because such a taper structure could not be fabricated with laser interference lithography (described in section 4.1).
Another disadvantage of using end-fire coupling is that only ω and the polarization can be set for the incoming beam; in other words, while this method would potentially allow us to couple to a mode with a frequency ω and certain assumed polarization properties, there is no way to set a specific k to couple to.
Detection of an excited guided mode can be done by Scanning Near-field Optical Microscopy (SNOM) [14]. Such detection perturbs the evanescent tail of a guided mode and thereby measures its spatial field distribution. This detection method is not preferable, however, since we are interested in the band structure rather than the field profile.

3.1.2 Grating coupling

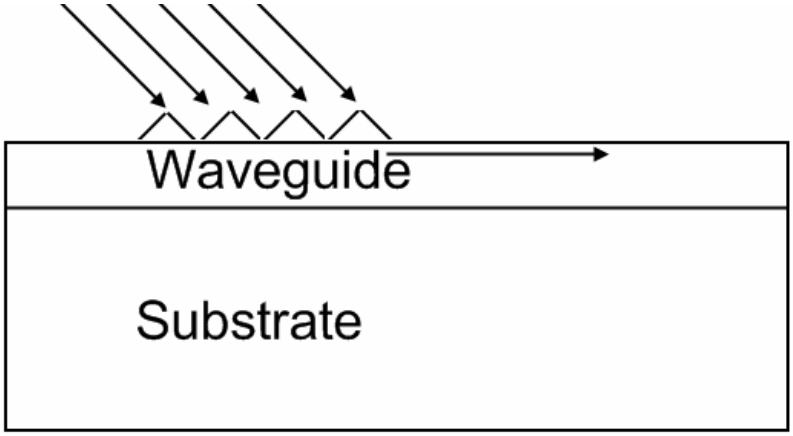

Figure 3.2: Grating coupler

As mentioned in the preceding section, incident out-of-plane radiation needs to be phase-matched to a guided mode in order for coupling to occur. One method to accomplish this involves placing a grating on top of the waveguide slab. The grating periodicity effectively adds an extra wave vector (the grating vector or multiples of it) onto a beam illuminating the grating, allowing it to be phase-matched to a PhC guided mode. [15]
However, this technique requires fabrication of a grating on top of the PhC slab. This coupling method was deemed unsuitable, since an additional grating on the PhC sample would have interfered with previous reflection- and transmission measurements and prohibits repeating or extending these types of measurements in the future.

3.1.3 Evanescent field coupling

As mentioned in the beginning of section 3.1, the reason why out-of-plane free-space radiation cannot couple to a guided mode is that it cannot be phase-matched; the k vector component in the plane of the slab of a free-space beam is simply too small. A suitable solution to this problem is to increase the incoming beam's k, which can be done by placing a high-index material on top of the PhC. This would effectively lower the light line. However, this would also drastically affect the dispersion and profile of the PhC's modes (see Fig. 3.3), as the top cladding material would no longer consist of air. Additionally, a strong coupling of incident light to modes of the PhC is a clear indication that these modes are no longer confined to the slab. In other words, the excited modes would no longer be truly guided.

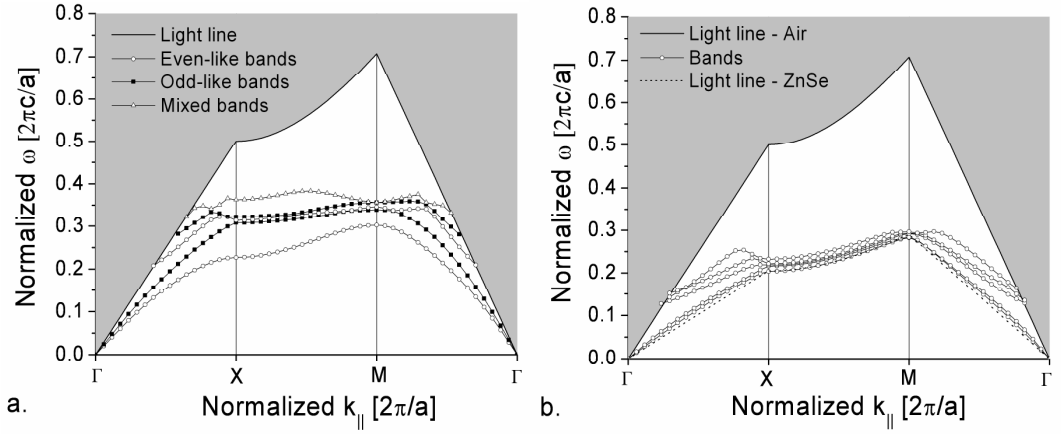

Figure 3.3: Band diagram (a) without and (b) with high-index top cladding

Fortunately, the high-index material does not necessarily have to be in contact with the PhC. As mentioned in section 2.3, a totally-reflected beam inside a high-index medium has an evanescent tail beyond the point of reflection. Now, if a medium with a totally-reflected beam is brought to a small distance d from the PhC, the evanescent tail resulting from the reflection will have a large spatial overlap with the guided mode. In the case that the evanescent tail has a $k_{\parallel}$ that matches a PhC guided mode, power can be transferred from the reflected beam to this PhC mode. This is sometimes referred to as "optical tunneling". This way, the modes of the PhC can be probed without inducing a large change in the PhC's band structure.

The theory behind this coupling mechanism will be more fully discussed in the next section, but for now it is of importance to note again that the projected wave vector inside the high-index (index n_p) medium, $k_{\parallel}$, must match the in-plane wave vector of a guided mode. This means that for coupling to occur, the input beam must be at an angle θ at the TIR interface such that, for frequency ω and the desired polarization (see section 2.3), the reflected wave is phase-matched to a PhC guided mode with a certain $k_{\parallel}$:

$$k_{\parallel,prism} = n_p k_0 \sin\theta = k_{\parallel,PhC} \qquad k_0 = \frac{n_{air}\omega}{c} \tag{3.1}$$

Eq. 3.1 indicates that for a given angle of the input beam, one ω-$k_{\parallel}$ pair is provided to probe the guided modes, providing a way to probe specific points in the band diagram. The angular dependence of the coupled $k_{\parallel,PhC}$ also indicates that, in an

experiment based on evanescent coupling, the resolution with which points in the band diagram can be determined depends on both the spectral resolution and the angular spread of the beam that is used.

Because of the wide range of k-vectors that can be set using such a setup, we have chosen to use this method for our coupling setup. Prior to providing further details on the choices made for the setup we will first discuss the evanescent field in the gap.

3.2 Theory of evanescent field coupling

We will start by discussing the evanescent field resulting from a totally-reflected beam in a high-index material. This evanescent field is mathematically described by an imaginary wave vector component perpendicular to the plane of reflection. This imaginary wave vector results in a time-averaged field amplitude that is exponentially decaying, rather than a propagating wave. This is shown in Fig. 3.4:

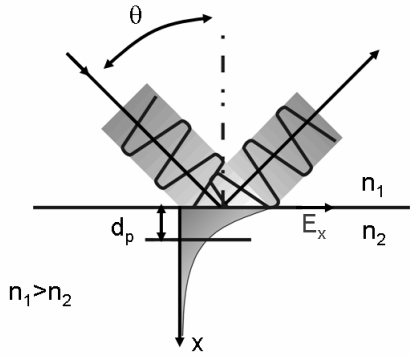

Figure 3.4: Evanescent field penetration

The extent to which this evanescent field penetrates the low-index material below the reflection is given by the penetration depth, d_p. This depth indicates the distance from the interface at which the electric field amplitude is 1/e times the amplitude at the interface and is given by Eq. 3.2. [16]

$$d_p = \frac{\lambda}{2\pi n_1 \sqrt{\sin^2\theta - \left(\frac{n_2}{n_1}\right)^2}} \tag{3.2}$$

As we wish to use the evanescent field to probe the guided modes of our PhC slab, this parameter is of critical importance. In order for a measurable transfer of light into the PhC mode to occur, the evanescent field needs to have sufficient overlap with the PhC mode. However, as stated in section 3.1.3, we wish to avoid disturbing the PhC mode profile. Therefore the distance between the reflecting medium and the PhC slab needs to be chosen such that the evanescent tail of the guided mode does not overlap too strongly with the high-index medium used for coupling. Otherwise, the guided mode would be modified, and resonances corresponding to coupling with the guided mode would broaden [17, 18, 19]. This means that the coupling distance d should be chosen sufficiently large, but small enough to achieve spatial overlap between the evanescent field from reflection and the evanescent part of the guided mode (Fig. 3.5).

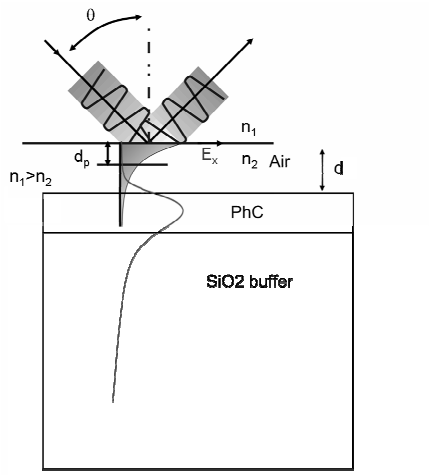

Figure 3.5: Evanescent field overlap

Time-inversion symmetry once again applies to optical tunneling through the evanescent field. In other words, if the evanescent field can couple light from a reflected wave into the waveguide, it can also couple light from a waveguide mode to a wave inside the high-index medium. To maximize the amount of power fed into a waveguide mode it is therefore necessary to remove the coupling prism right behind the point where power is fed into a waveguide mode, thereby avoiding that the mode couples out again. For this reason, a right-angle prism is frequently used (Fig. 3.6). By aiming the incoming beam at the prism's right angle and by carefully controlling the distance d between prism and slab, as much as 80% of the incoming beam's power can be transferred to waveguides [17].

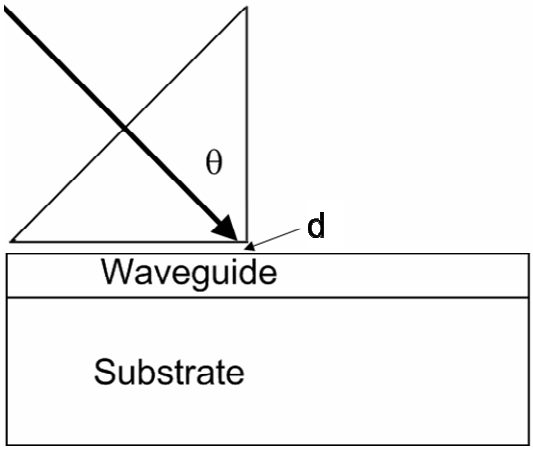

Figure 3.6: Coupling with a right-angle prism

3.3 Attenuated Total Reflectance

Now that we have described the properties of the evanescent field, we will discuss practical methods for probing the PhC's guided modes. In order to detect coupling to the PhC modes, it is convenient to measure the intensity of the reflected beam rather than attempting to directly measure the excitation of a PhC mode. If at a certain angle θ and frequency ω a lower reflected power is measured than at other angles and frequencies, this indicates the presence of a mode with ω and $k_{\parallel}$ as given by Eq. 3.1. This principle is called attenuated total reflectance (ATR).
A number of different high-index geometries can be considered for ATR-based measurement techniques. In the seminal paper by Tien, Ulrich and Martin [20], a high-index flat-faced prism was used as the ATR prism. Furthermore, a technique that was later named "m-lines" was used: by focusing the incoming beam on the base of the prism, a range of angles θ was probed simultaneously, as shown in Fig. 3.7.

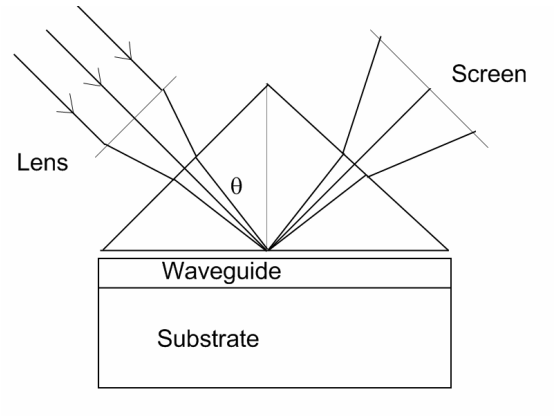

Figure 3.7: m-lines

In this case, coupled modes are visible on the screen on the right-hand side as dark lines. This system of simultaneous excitation is not the only possible way to measure the coupling parameters, however. A viable alternative is to shape the incoming beam so that it has a low angular spread when it hits the prism base. The coupling parameters can then be determined by changing the reflection angle θ (and hence changing $k_{\parallel}$) and measuring the reflected power with a fixed frequency of incident light. Alternatively, a spectral scan can be performed at a fixed angle, thereby changing ω while keeping $\frac{\omega}{|k|}$ fixed.

Until now we have discussed coupling geometries using flat-faced prisms. However, these flat-faced prisms have one major disadvantage: the internal angles of the prism will limit the range of θ values that can be set [21]. This is due to refraction of the probe beam upon entering the prism. We have therefore chosen to use a hemispherical prism (Fig. 3.8). The advantage of this geometry is that any angle ranging from the total internal reflection angle of the medium to almost-glancing incidence can be used.

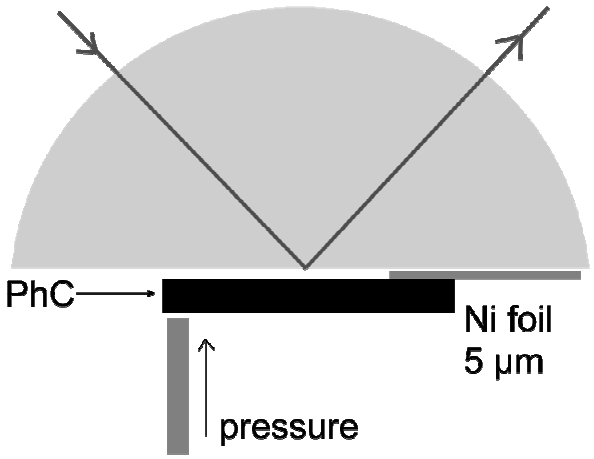

Figure 3.8: ATR with hemisphere and distance control

A disadvantage of this ATR coupling geometry is that coupling is expected to occur over a relatively broad area, unlike the coupling scheme shown in Fig. 3.6. In practice, this could cause the eventually measured ATR signal to also contain light that was coupled into the crystal and then coupled out again, instead of containing only the directly-reflected light. This could result in spectral measurements similar to those obtained by specular reflectivity measurements, exhibiting a Lorentz-Fano lineshape [10, 11, 30, 31]. However, this effect is expected to be weak, since an excited guided mode is expected to be damped heavily due to crystal irregularities and is not expected to couple out significantly. Therefore the lineshape is expected to be predominantly Lorentzian.

3.4 Distance control

As mentioned in the previous section, the coupling distance d between sample and medium is a critical parameter which needs to be adjustable on a scale of d_p (Eq. 3.2). For such an adjustment, practical prism coupling setups for unpatterned slab waveguides regularly employ a pressure point in close vicinity of the reflected spot. By adjusting the pressure, the coupling distance can be controlled, with the added advantage that the sample is slightly deformed and does not have a uniform coupling over the entire prism base (Fig. 3.9). This non-uniform coupling distance can be regarded as weakly resembling the decoupled case of Fig. 3.6.

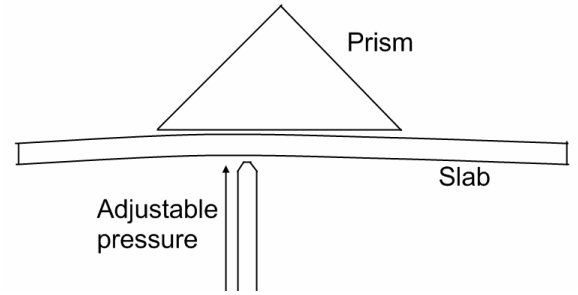

Figure 3.9: Distance control by pressure point

However, as our sample contains an array of holes, it was feared that pressing the sample against the ATR medium would cause damage to the PhC layer.
An alternative method to control separation between sample and hemisphere is the use of three piezoelectric actuators [22]. Such a setup allows for fine control over the separation distance d as well as alignment between hemisphere and sample surfaces. It should be noted that these methods do not provide any information on the absolute value of the separation distance; rather, this distance can be obtained by fitting rigorous coupled wave analysis (RCWA) simulations to measured data. [34]
For our setup, we opted to induce a deformation in the sample by clamping it against the hemisphere on one end, and placing a piece of 5 µm Ni foil between sample and hemisphere on the other end. (Fig. 3.8)
In order to obtain detailed information on the expected deformation of the sample, a 2D simulation was performed using a finite-element calculation of the static plane strain (COMSOL Multiphysics [23]). For this simulation, a number of approximations were made. The sample was assumed to consist entirely of crystalline silicon (525 µm thick). The clamping was modeled as a line constraint; this area (1.5 mm wide) was assumed to have zero distance to the hemisphere. The Ni foil was modeled as a point constraint; a point laying 1 mm from the right-hand edge of the sample was assumed to be 5 µm below the hemisphere. The result of this simulation can be found in Fig. 3.10.

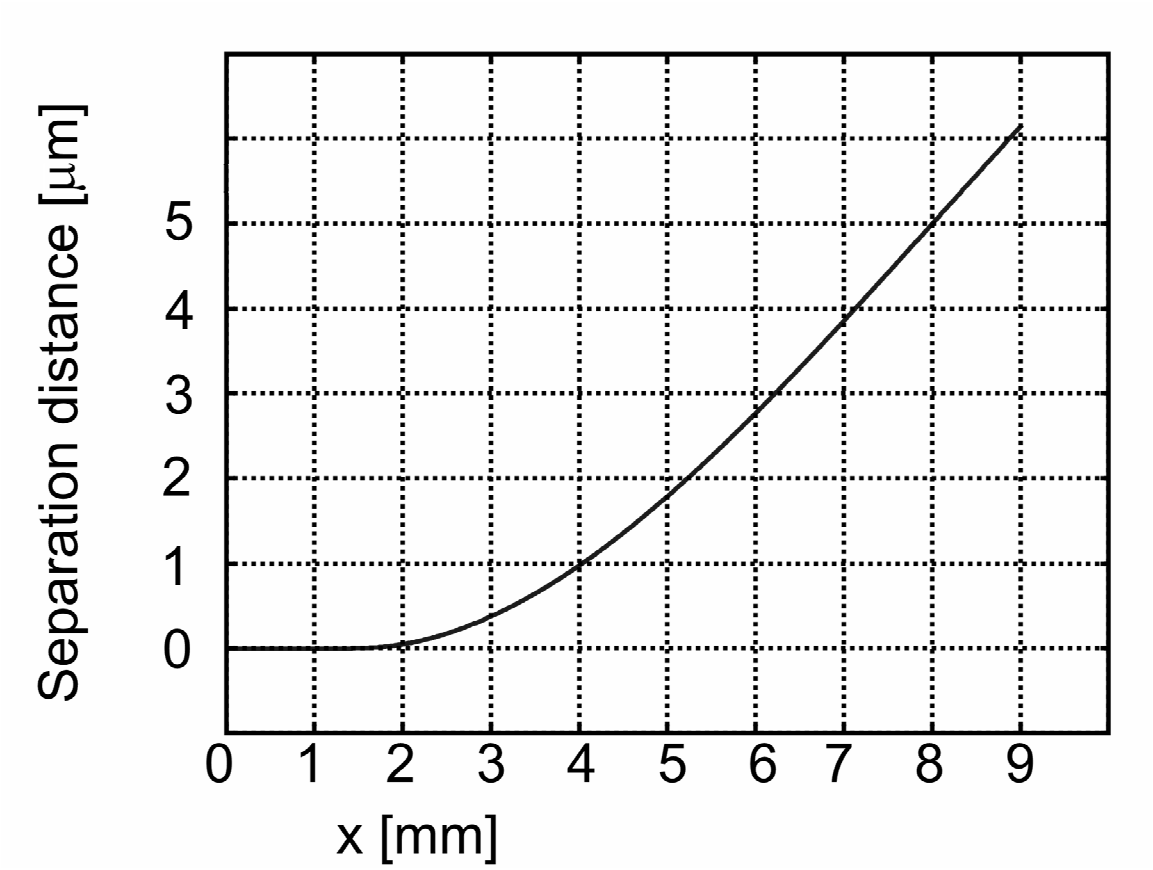

Figure 3.10: Deformation of sample

As can be seen in this figure, the distance between ATR prism and PhC can be controlled by moving the point of reflection relative to the pressure point (Fig. 3.8). This allows for a distance d to be set between practically zero (dependent on cleanness of sample and ATR prism) and 5 µm, i.e. from 0 to 1.5 wavelengths (assuming a vacuum wavelength of 3.3 µm). This means that the induced bending deformation should allow for the coupling distance d to be controlled on the scale that is required, as was stated at the beginning of this section.

4. Experimental aspects

This chapter presents an overview of the experimental setup used to obtain the results discussed in chapter 5. We will start by discussing our sample's design and fabrication in some detail. In Section 4.2 the reasons for using and the operational principles of the optical parametric oscillator (OPO) will be discussed. The characteristics of the OPO will be detailed and its properties as obtained by experimental measurements will be presented. An overview of the complete measurement setup is discussed in section 4.3.

4.1. PhC design & fabrication

This section briefly describes the design and fabrication choices that were made when the PhC sample under investigation was fabricated. The intended design of the sample is shown schematically in Fig. 4.1. A scanning electron micrograph (SEM) of the fabricated sample is shown in Fig. 4.2. The Si substrate (522 µm) below the SiO_2 layer is not shown in either figure.

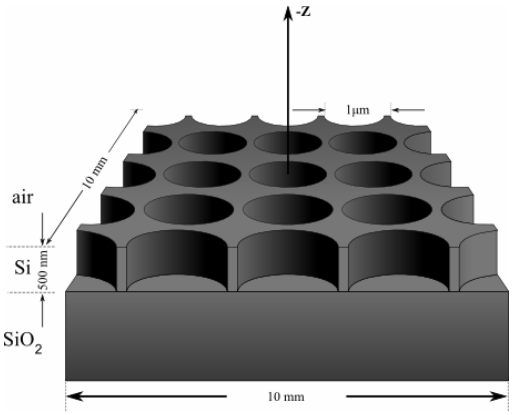

Figure 4.1: Sample design schematic

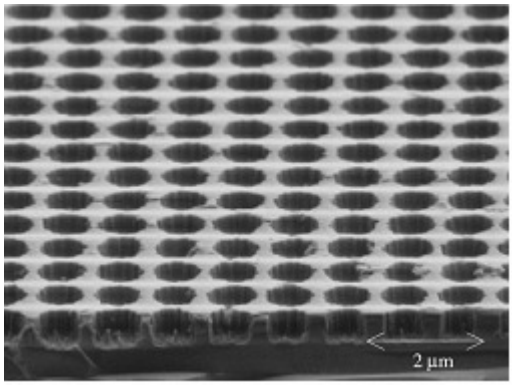

Figure 4.2: SEM micrograph

As can be seen in Fig. 4.2, a square lattice of air holes in a Silicon-on-Insulator (SOI) wafer was fabricated. We will now discuss the reasons behind this design, starting with the choice to use silicon.

As stated in chapter 1, our sample was designed for possible applications that make use of third-order optical effects. This means that the high-index material used to fabricate the PhC needed an appreciable third-order refractive index as well as a high optical damage threshold [6]. Silicon (Si) was chosen for this. GaAs, which is a frequently-used alternative to Si, offers an approximately tenfold higher third-order response (Table 4.1). However, there was no infrastructure for GaAs fabrication available to us, and thus we decided to fabricate the 2D PhC slabs from silicon. As the photonic layer has a thickness smaller than the vacuum wavelength of the principal guided modes (in our case, 0.5 µm – see Fig. 4.1), a substrate is necessary to support a large-area PhC. This makes Silicon-on-Insulator (SOI) the preferred geometry. A great advantage to this is that SOI wafers are already used for integrated electrical circuits, such as the processors by Advanced Micro Devices, Inc. (AMD). This means

that SOI technology is an attractive candidate for possible future integration of optical and electrical circuits.

Table 4.1: Si vs GaAs

	Si (crystalline)	GaAs
MIR Refractive index n_0	3.4	3.3
Third-order refractive index n_2 (cm^2/W) [24]	2.7×10^{-14}	3.3×10^{-13}
Electronic band gap at 300 K (eV)	1.11	1.42
Thermal conductivity ($W\ cm^{-1}\ K^{-1}$)	1.3	0.55

It was previously shown that both the Kerr effect and two-photon absorption can be used to switch a Si/SiO_2 multilayer mirror, but it was suggested that a larger PhC made out of silicon with air holes would exhibit stronger switching effects [25] due to a sharper band edge and a larger refractive index contrast.
As stated before, Si has an electronic band gap of 1.11 eV. This means that for incident wavelengths below 2.25 µm, two-photon absorption can take place. Upon absorption of two photons, electrons are excited from the valence band to the conduction band, thereby injecting free carriers into the conduction band. These free carriers cause an effective change in the material's refractive index. As the band structure of a PhC slab is highly dependent on the refractive indices of the materials it is composed of, this optically induced index change can be used to, e.g., move the position of the stop gap.
The lifetime of these free carriers can be as high as 100 µs [26] in crystalline silicon, while a purely $Re(\chi^{(3)})$, or Kerr-effect, response would be in the fs regime. This means that in the two-photon absorption case, the maximum switching frequency would be limited by the free carrier lifetime; therefore, for fast all-optical switching, two-photon absorption needs to be avoided.

To avoid carrier transport, the PhC structure was designed to have a stop gap around 2.5 µm. This can be achieved with a square lattice of air holes, pitched 1 µm apart. While a square lattice can never have a complete band gap [2], there are advantages to using this geometry rather than a triangular lattice. It has been shown [27] that disorder in a triangular lattice has a larger effect on the (spectral) broadening of modes, while for a possible switching application sharp band edges are desired. Furthermore, in the case of a defect waveguide (absent in our structure, but of interest for future applications) a square lattice surrounding the defect would present losses an order of magnitude lower than those in a triangular-lattice defect [28]. The absence of a complete band gap is not actually a problem when regarding switching applications, as light that needs to be switched generally has a well-defined direction and polarization.

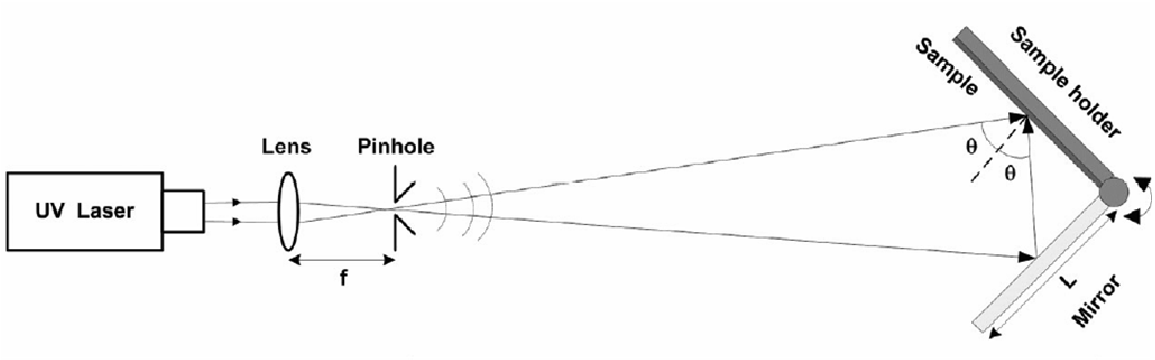

Figure 4.3: Laser Interference Lithography

For the fabrication of the crystal, a SOITEC [29] SOI wafer was used. In order to fabricate a pattern with the design parameters mentioned above, a novel modification of Laser Interference Lithography (LIL, see Fig. 4.3) [13] was used, allowing this technique to be used for patterning high-index materials such as silicon. For LIL, the wafer was first coated with a photoresist layer. For transferring the desired pattern to the photoresist layer, two superimposed UV laser beams with a large (3 cm^2) cross section were used. The standing-wave pattern resulting from interference between the two laser beams is used to create a striped pattern. A second exposure, with the wafer rotated by 90°, results in the final square pattern of holes, as only the spots lying on intersections between the standing-wave pattern stripes have received an exposure above the resist's threshold. By a number of etching steps [13] this pattern was then transferred to the top Si layer of the SOI wafer. The LIL fabrication method was chosen because it allows for a well-defined large-area periodicity. This property is of importance to filtering applications [11, 12] but it also ensures that the sample has a well-defined band structure over its entire area. A detailed comparison between LIL and other fabrication methods can be found in various publications by Prodan *et al.* [10, 12, 13, 31]
After fabrication, a rectangular sample (9.5 x 8.0 mm) was cut out of the wafer. The previous optical characterization that was performed has already been briefly described, in section 2.5.

4.2 MIR radiation source

As described in chapter 1 and 2, guided modes in the mid-infrared (MIR) spectral range, with photon energies less than half the electronic band gap of silicon, are of special interest for future non-linear optical applications. As the aim of our experiment was to probe these guided modes, a tunable source of MIR radiation was needed. While specular reflectivity measurements [10, 11] had earlier been performed with the same crystal using the spectrally-filtered output from a Quartz-Tungsten-Halogen (QTH) lamp, that method suffers from a poor spectral power density as only 2 nW of power with 5 nm (~400 GHz) spectral bandwidth around a wavelength of 2 µm was available for measurements [10]. Furthermore, that experiment could only be used to couple to the "leaky" modes of the PhC, which are above the light line (see chapter 2). As these modes are spectrally broad due to their lossy nature, the filtered QTH source provided sufficiently narrowband radiation. Measured spectral resonances exhibited a Lorentz-Fano profile [10, 11, 30, 31]. However, in the case of guided modes below the light line, there are no intrinsic losses. This means that the spectral features of guided modes are only broadened by extrinsic losses [12, 31] and the presence of the ATR coupling medium [18, 19], though the amount of broadening is not known. Based on the extrinsic contribution to the spectral width of specular reflectance features measured earlier [12, 31] we can estimate a minimum amount of broadening. We assume that the extrinsic losses of the guided modes probed in this experiment are comparable to the extrinsic losses of the leaky modes that were previously measured. This assumption is only valid if the field distribution inside the PhC associated with a leaky mode is similar to the field distribution associated with a guided mode. Based on these previous measurements we expect the spectral width of ATR features to be at least $\frac{\Delta\omega}{\omega} = 10^{-3}$. Using an incident vacuum wavelength of 3 µm, a spectral resolution better than 100 GHz is needed to resolve resonances. While increasing the spectral resolution of the filtered QTH source is possible by decreasing the angular spread of the light entering the monochromator [11], this would significantly reduce the output power. Furthermore, the collimator lens in the available QTH lamp (Oriel 66995) has a reduced transmittance for wavelengths larger than 2.5 µm, requiring lock-in amplification with prohibitively long integration times to obtain a sufficiently high signal-to-noise ratio (SNR). Therefore, it was decided to look for an alternative, tunable source of MIR radiation with a higher spectral power density and a high (diffraction-limited) spatial beam quality.

High spectral power density (i.e., a narrow spectral bandwidth) and a high spatial beam quality in the MIR can be obtained from optical parametric oscillators (OPOs), especially continuous-wave (CW) singly-resonant OPOs (SRO). Therefore, we selected such a device as the MIR source to perform our measurements. The operational principle of an OPO as well as the properties of the OPO that was used will be discussed in the next section.

4.3 MIR OPO

Here, we will briefly discuss the parameters of importance for the operation of an OPO, as the OPO used was employed as a tool and was not the focus of our research. As it is beyond the scope of this thesis to provide an in-depth theoretical treatment of OPOs and nonlinear optics, the reader is referred to a textbook on nonlinear optics (e.g., [4]).

An OPO essentially converts incident high-frequency light ("pump") to two lower frequencies ("signal" and "idler", the signal being by convention the shorter wavelength of the two). This conversion process obeys energy conservation: the energy of one pump photon equals that of the signal plus the idler photon.

$$\omega_p = \omega_s + \omega_i \tag{4.1}$$

To ensure a net gain of signal and idler waves, phase matching (or "momentum conservation") is of importance for efficient conversion. This condition can be stated as:

$$\vec{k}_p = \vec{k}_s + \vec{k}_i \qquad \left|\vec{k}(\omega)\right| = \frac{\omega n(\omega)}{c} \tag{4.2}$$

Phase matching is by no means trivial, as normal dispersion of practically all materials implies that $n(\omega_p) > n(\omega_s) > n(\omega_i)$, meaning that Eq. 4.2 cannot be satisfied. To overcome this problem, birefringent phase matching (BPM) can be used in some OPOs at particular wavelengths. This phase matching method relies on the crystal having an anisotropic refractive index and the pump, signal and idler waves being polarized along different directions. A disadvantage of BPM is that the $\chi^{(2)}$ coefficient is generally much lower for such non-parallel polarizations, resulting in a lower conversion efficiency. Another effect which limits the efficiency of a BPM-based OPO is walk-off. Because the pump, signal and idler beams do not propagate in exactly the same direction, the crystal length over which the waves are spatially overlapping in the crystal is limited. As a longer crystal length results in a higher efficiency, this limit is undesirable.

To avoid these problems, quasi-phasematching (QPM) is used in many OPOs. This method relies on periodically changing the sign of the second-order response $\chi^{(2)}$ of the OPO crystal. This is usually accomplished by alternating periodically between two crystal orientations, with a period of Λ. This, in effect, adds another wave vector to Eq. 4.3:

$$\Delta k = \vec{k}_p - \vec{k}_s - \vec{k}_i - \vec{k}_{QPM} \qquad |\vec{k}_{QPM}| = \frac{2\pi}{\Lambda} \tag{4.3}$$

QPM has important advantages over BPM. All three waves in the OPO can be chosen to be polarized parallel to each other and propagate along the same path. Therefore, the efficiency of a QPM-based OPO is generally much higher than that of a BPM-based OPO. Also, when using BPM, the wavelength range over which phase matching can be achieved is limited by the crystal's natural birefringence, while QPM allows any pair of wavelengths to be generated by choosing the appropriate Λ and thereby $\vec{k}_{QPM}$ during crystal fabrication, provided the crystal is transparent for the intended wavelengths. Nonlinear optical crystals with a QPM period are readily available. It will therefore be assumed that QPM will be used.

Another critical parameter for the operation of OPOs is that of cavity resonance. For parametric oscillation, it is necessary for the cavity to be resonant for at least one of the waves. In this case, the OPO is called singly-resonant (SRO) which provides the advantage of maximum freedom of tuning.

In a SRO, the signal frequency is generally chosen as resonant. Any pair of frequencies $\omega_s + \omega_i$ can be generated from a pump beam, provided Eq. 4.1 is fulfilled and provided the phase mismatch (Eq. 4.3) is small enough. Because the signal wave is resonant, modes other than the one with the smallest Δk are suppressed after a few cavity round trips of the signal wave, as the $\omega_s + \omega_i$ pair with the highest signal power inside the OPO cavity will have the most gain. Additionally, by placing a frequency-selective element inside the OPO cavity, a single signal wavelength can be selected. An example of such an element is an etalon. Provided a sufficiently narrowband pump source is used, a CW SRO can be used to generate narrowband radiation in a single spectral mode, meeting the first requirement stated earlier.

Finally, the light source for this experiment needs to be tunable over a wide frequency range. To achieve tuning, a number of parameters can be changed, such as the pump frequency (Eq. 4.1). The widest tuning range can usually be achieved via the parameters that change phase matching, in Eq. 4.2 and 4.3. In the case of QPM, one such parameter is the poling period Λ, i.e., when several poling periods are available in the same nonlinear crystal, then by repositioning the crystal in the OPO cavity, a different poling period can be selected, changing Eq. 4.3.

Finally, the crystal dispersion can be altered, and thus the output wavelength can be tuned by temperature-induced changes of the refractive indices for the various waves inside the crystal (Eq. 4.2). For this purpose, OPO crystals are typically placed inside a temperature-controlled oven.

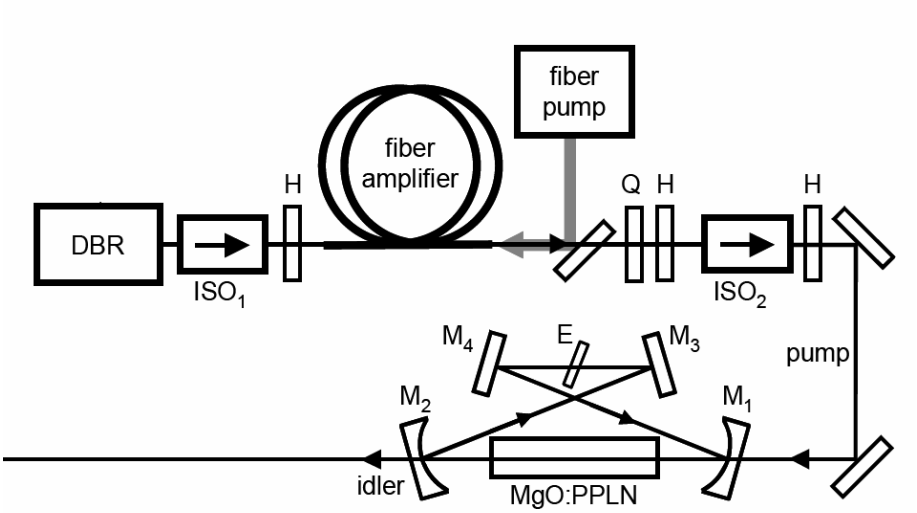

Figure 4.4: OPO schematic (taken from [32]), M: mirror, H: half-wave plate, Q: quarter-wave plate, E: Etalon, ISO: isolator

We now briefly discuss the properties of the OPO that was used for our experiment [32], shown schematically in Fig. 4.4. A master oscillator power amplifier (MOPA) configuration is used to pump the OPO. The basis for this pump source is a multi-

section distributed Bragg reflector (DBR) diode laser, which provides 50 mW of output power in a single spectral mode (30 MHz linewidth, output wavelength 1062 nm) and can be continuously tuned over ranges in excess of 100 GHz. The output from this diode is then amplified by an Ytterbium-doped fiber amplifier, which in turn is end-pumped by a 30 W 976 nm diode bar. The basis for this OPO is a ring (or "bow-tie") cavity. The mirrors used for the OPO are highly reflective for the intended signal wavelengths, between 1.5 and 1.6 µm. For conversion of the pump beam, a periodically-poled Lithium Niobate crystal doped with MgO (MgO:PPLN) is used. The crystal contains poling periods ranging from 28.5 to 31.5 µm. The crystal is placed in an oven controlled by a temperature controller to allow for temperature tuning. An etalon is available to limit the OPO operation to a single mode.

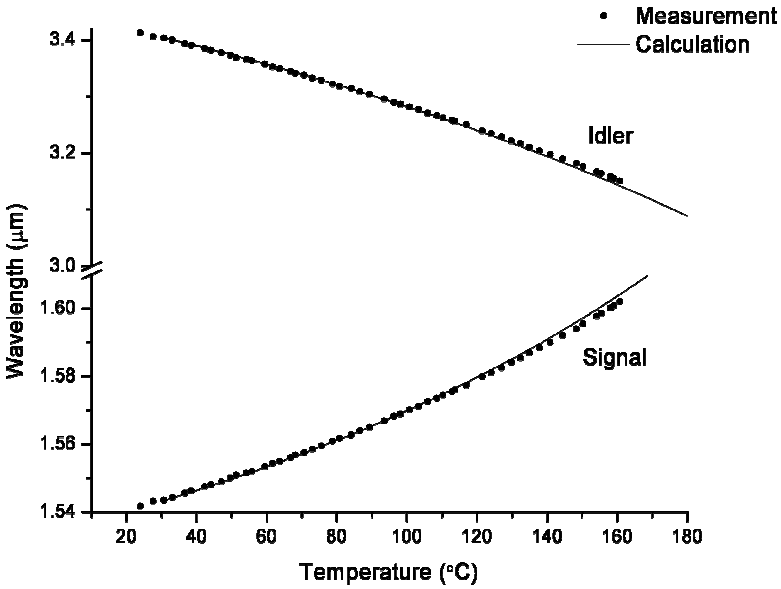

Figure 4.5: OPO temperature tuning curve, Λ =30 µm

As a test of temperature tuning of the output wavelength, we measured the signal wavelength as a function of the crystal temperature, using the optical spectrum analyzer mentioned in section 4.4. The idler wavelength was calculated using Eq. 4.1. The temperature tuning characteristics of the OPO, using Λ=30 µm poling period, can be found in Fig. 4.5. A good fit was found between the expected tuning curve (based on refractive index data [35]) and the experimental data. The limits of the tuning range are dependent on the frequency range within which the OPO mirrors are highly reflective for the signal wavelength.

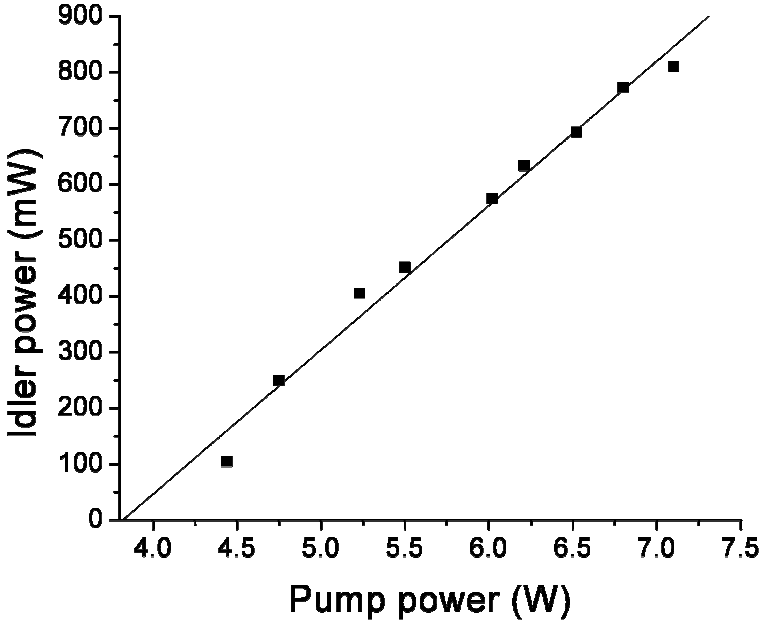

Figure 4.6: Idler power vs pump power for idler=3236 nm

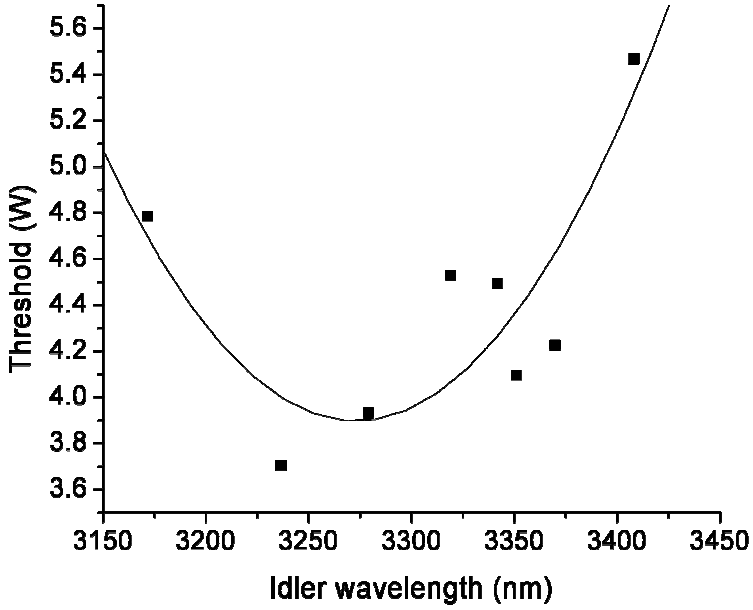

Figure 4.7: OPO Threshold vs Idler wavelength

As an additional characterization of the performance of the OPO, we measured the idler output power as a function of the pump power. Typical results are displayed in Fig. 4.6 for a fixed idler wavelength and it can be seen that, indeed, the OPO provides a MIR output which is many orders above that achieved by spectral filtering of while-light (lamp-type) sources.

Finally, the OPO was characterized with regard to its oscillation threshold vs. the idler wavelength to be generated. This data is displayed in Fig. 4.7 and shows that the threshold varies (within the tuning range of Fig. 4.5) from about 4 to 5.5. W. However, as the available pump power was more than 7 W, the generated MIR output was always several 100's of mW, which is more than sufficient for the measurements intended with the PhC.

4.4 Overview of the experimental setup

As was discussed in section 3.3, a hemispherical prism was chosen as the ATR medium, which gives access to a wide range of total internal reflection angles, corresponding to a wide range of in-plane wave vectors that could be probed (Eq. 3.1).
Hemispheres for ATR are commercially available. For our setup, we chose a ZnSe hemisphere (Harrick Scientific EM6XBB [33]). The choice for ZnSe is motivated by its high refractive index of 2.44 for a vacuum wavelength of 3 μm and its transparency in a large wavelength range, starting in the visible range and extending well into the MIR (between 0.5 and 20 μm). While using a material with an even higher index (such as Si or Ge) would have allowed coupling to modes with a higher $|k_{\parallel}|$, these materials are opaque for visible light which complicates alignment.

The aim of this experiment was to probe the guided modes of our PhC. As discussed in section 4.2, our MIR OPO provides radiation with a high resolution in the frequency domain and high spatial quality. Since we aimed to obtain both ω and $\vec{k}$ corresponding to a guided mode with a well-defined wave vector, the reflected beam inside the ZnSe sphere needs to have a low angular spread.

To achieve these goals we have used the setup as shown in Fig. 4.8. Lens positioning was calculated by means of ABCD matrices [4], with the beam divergence measured just behind the OPO as the input parameter. In order to minimize the angular spread at the point of (ATR) reflection, this reflection was made spatially symmetric, i.e., the spatial distribution of the beam as a function of the distance from the ATR reflection was carefully adjusted such that this distribution was the same before and after the ATR reflection. This was done by positioning the second lens (f=15, see Fig. 4.8) such that two foci were created 5.5 mm from the surface of the ZnSe hemisphere. Based on the accuracy with which the positions of these foci could be measured, the reflection was estimated to have an angular spread of less than 0.2˚.

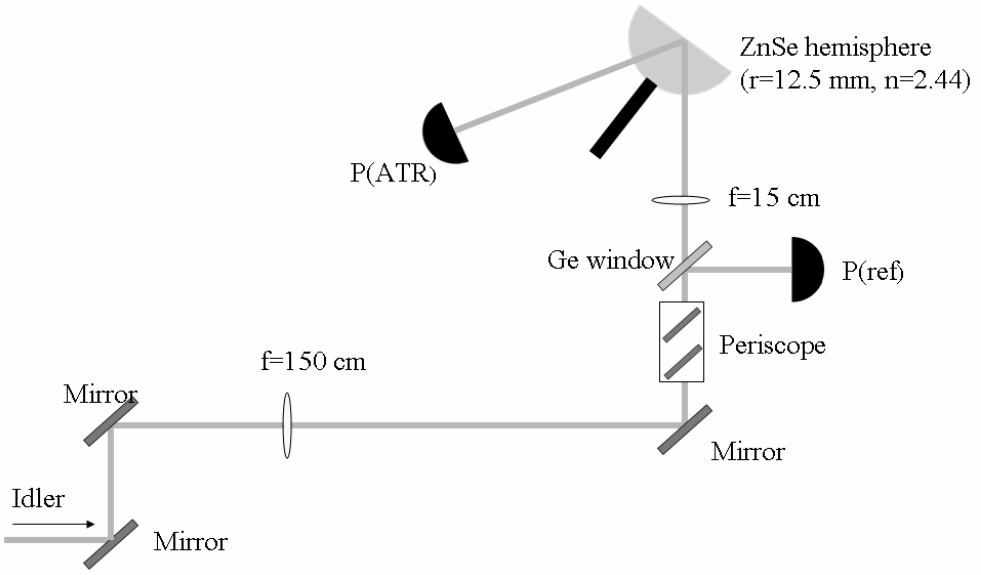

Figure 4.8: Measurement setup

The output of the OPO is linearly polarized normal to the main surface of the PPLN crystal in the OPO. In order to probe both TE-like and TM-like modes in the PhC, the beam's polarization must be rotated. Since a λ/2 plate was not available for the wavelength range under investigation, a periscope was used to rotate the polarization by 90˚.
To orient the PhC with respect to the ATR reflection plane and incident polarization, a plastic sheet was attached to the PhC sample indicating crystal symmetry directions (see Fig. 4.9). The symmetry directions were obtained using the diffraction pattern from a normal-incidence reflected HeNe laser beam.
Because the OPO idler output power was observed to fluctuate in time, simultaneous measurements of reflected (ATR) power and idler power were required. For this purpose, the OPO idler beam was split using a Germanium window to allow simultaneous measurement of the ATR signal, indicated by P(ATR), and the idler power, indicated by P(Ref).
Power meters (Newport 818P-030-19 and Newport 818P-010-12) were used, integrating measurements over 30 seconds. Measurements show that with a 30 second integration time, the standard deviation due to noise was less than 4%. Using a 60 second integration time, this standard deviation was less than 2%. During measurements, incident background radiation levels were checked periodically by blocking the idler beams. The signal wavelength was monitored continuously using an optical spectrum analyzer (ANDO AQ-6315A) which has a resolution better than 10 GHz in the idler wavelength range.

To find the PhC's guided modes, a large frequency range needed to be scanned. Furthermore, as the OPO output wavelength was tuned in steps, there was a chance narrowband resonances would be missed during a measurement. To avoid this, we attempted to broaden the expected spectral resonances by choosing a small coupling distance d (see section 3.4). A coupling distance of 400 nm was chosen, corresponding to x=3 mm in Fig 3.10. The amount of broadening induced by the presence of the ZnSe sphere could not be calculated due to limitations in the available RCWA software (see section 3.4). However, based on similar measurements [18] this broadening was estimated to be at least $\frac{\Delta\omega}{\omega} = 5 \cdot 10^{-3}$ FWHM, corresponding to a bandwidth of ~450 GHz. Because at a distance $d = 0$ the presence of the sphere will make all the modes leaky, the maximum broadening that was expected to occur is that of a typical leaky mode as was determined previously by us, $\frac{\Delta\omega}{\omega} = 2.5 \cdot 10^{-2}$ [10, 11, 31], therefore the maximum bandwidth of ATR resonances is expected to be 2 THz FWHM. This is consistent with the bandwidth of resonances measured by Galli *et al* [18]. According to their measurements, the relative drop in reflectance corresponding to guided mode coupling ranges from 10-70%.

Using the configuration described above, reflectance spectra were measured by temperature-tuning the OPO. Mode hops were observed during the measurements, but these were measured to span only a small bandwidth of less than 35 GHz. As this bandwidth is much smaller than the expected bandwidth of the features in ATR spectra, these mode hops are not expected to pose a problem. Temperature increments were chosen such that the OPO idler output was changed in steps of 150 GHz. These increments were chosen sufficiently small to ensure spectral features would not be missed, but sufficiently large to avoid prohibitively long measurement times.

The measurements that were performed using the setup described in this section, will be discussed in the next chapter.

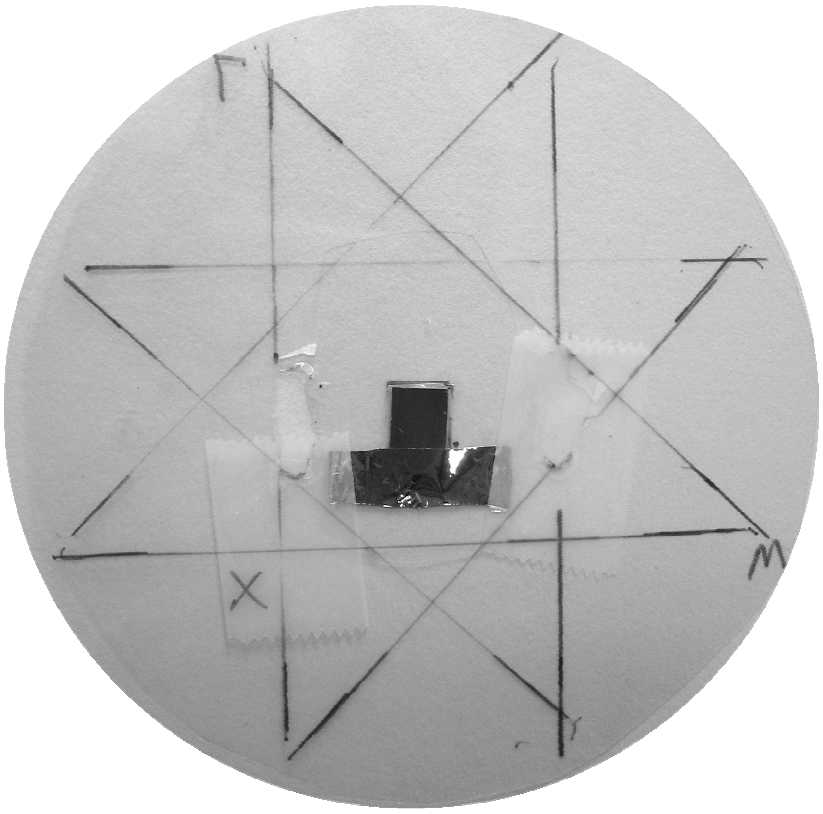

Figure 4.9: PhC and attached plastic sheet

5. Experimental results & discussion

This chapter compares the expected coupling parameters (angle and frequency), based on the calculated band diagram, with the measured ATR curves. It appears that, indeed, coupling to guided modes was observed, although measurements over a larger spectral range would be required for further confirmation.

5.1 Expected coupling parameters

We will start by discussing the expected coupling angles based on the theoretical band diagram presented in chapter 2. We will only examine PhC bands crossing the idler output range of our OPO. Within the poling period used, the idler output wavelength could be tuned from 3.15 to 3.41 μm (see Fig. 4.6). This corresponds to a normalized frequency range from 0.293 to 0.317.
Fig. 5.1 shows part of the theoretical band structure in the Γ-X and Γ-M symmetry directions, showing both the first and the second Brillouin zone. The probe light beam from the OPO forms a certain reflection angle internal to the ZnSe hemisphere. By varying the frequency of the OPO for a fixed angle, one scans over a range of ω and $k_{\parallel}$ values as calculated using Eq. 3.1. Also, by varying the internal reflection angle for a fixed OPO frequency, different projected $k_{\parallel}$ values can be probed. Because of the way the ZnSe prism and the sample were mounted, internal reflection angles in the range 35-75° were accessible. Figure 5.1 shows a number of these scan ranges as dashed lines for several reflection angles inside the ZnSe ATR prism. Coupling is expected at the intersection of these lines with the dispersion curves of the PhC.

As can be seen in Fig. 5.1b, TM-like (odd mode) features in a Γ-M ATR spectrum are expected to occur only for $\theta < 44°$. The band corresponding to this resonance (lying in the first Brillouin zone) is expected to have a steep dispersion, the slope of which is close to that of the dispersion of the probe beam. Therefore, coupling resonances are expected to be too broad to be resolved within the OPO tuning range. A single TE-like (even mode) band is expected to be present within the probing range, but since this band only crosses a limited part of the OPO tuning range, it is expected that this band can possibly lie outside the tuning range of the OPO. It was therefore decided to limit initial measurements to the Γ-X symmetry direction.

As can be seen in Fig. 5.1a, Γ-X ATR spectra measured at angles between 45 and 55 are expected to show features corresponding to mode coupling. For the angular spread estimate of the ATR reflection given in section 4.4, broadening of spectral features due to this angular spread was estimated to be less than 300 GHz, which corresponds to a wavelength interval of less than 9 nm in the wavelength range under investigation. The various expected spectral broadening effects that were described in chapter 4 are summarized in Table 5.1.

Table 5.1: Expected broadening effects

Broadening effect	$\Delta\omega$ **(GHz)**
Angular spread of the beam	300
OPO bandwidth and mode hops	25
Scattering losses	100
ATR prism mode perturbation	450 to 2000
Total expected spectral width:	875 to 2425

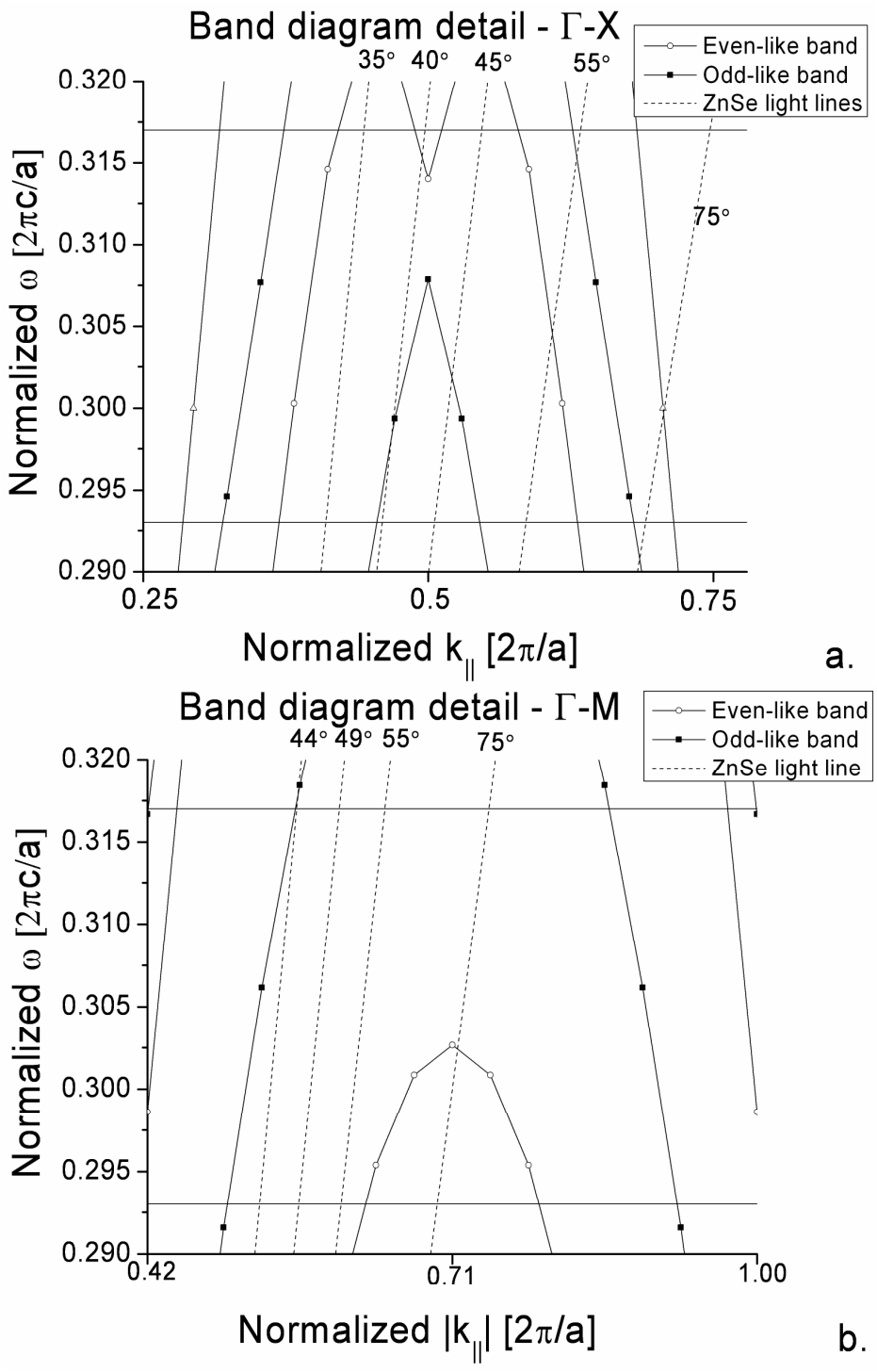

Figure 5.1: Band diagram detail, first and second Brillouin zone, a) Γ-X , b) Γ-M

5.2 Experimentally obtained ATR spectra

Spectral scans were performed both for TE- and TM polarizations, expected to couple to even and odd modes as discussed in section 2.3. A number of ATR spectra can be found in Fig. 5.2. Frequencies where spectral features are expected to show have been indicated in the figure by grey circles. The TE spectra measured for $\theta = 35°$ and $\theta = 37°$ were measured using a detector integration time of 60 seconds, while the other spectra were measured using an integration time of 30 seconds. As the spectra obtained with the longer integration time show a much flatter spectrum, it can be concluded that the noise measured is caused by random noise from the surroundings.

Three of the spectral scans show features of note, as is indicated by arrows, where the reflectivity deviates from a spectrally constant value (indicated by dashed lines) by more than the experimental error (indicated by the vertical bars near the vertical axis). The first feature that should be noted is the drop in reflectivity for TE at $\theta = 35°$, indicated in Fig. 5.2a. However, at this angle, the OPO beam crossed some glue residue from the ATR prism mount (see Fig. 4.5) which makes it possible that these spectral features correspond to absorption by the glue rather than mode coupling. The exact same drop in reflectance was also observed in a spectrum measured using TM- rather than TE-polarized light at the same angle (not shown in Fig 5.2b). As the same feature was measured for both polarizations, we attribute this drop to absorption of the probe light by the glue.

The measured TM spectrum for $\theta = 45°$ (Fig. 5.2b) shows a drop in reflectance for longer wavelengths. As this drop is much larger than the experimental error (noise) observed in other measurements, it can be attributed to guided mode coupling. Furthermore, the expected probe wavelength for coupling is 3325 nm (indicated by a grey circle in Fig. 5.2b), which is approximately the range where the measured reflectivity is noticeably lower. However, the expected center wavelength does not coincide with a minimum in the measured reflectivity. This could possibly be explained by bands being shifted to lower frequencies, as was qualitatively shown in Fig. 3.3. The width of the detected reflectivity drop is in fact larger than the range covered by the OPO. Therefore, we were unable to resolve the complete feature and can only estimate its FWHM bandwidth based on this trace. Assuming that the feature has reached a minimum reflectance near the end of the OPO tuning range, we estimate that the feature has a FWHM bandwidth of at least 4 THz. A similar feature was observed using incident TE light, for $\theta = 55°$.

The two features mentioned above have a bandwidth larger than what was expected, spanning at least 4 THz as compared to the estimated maximum bandwidth of ~2.4 THz (see Table 5.1 as well as section 4.3). This would indicate either that the coupled modes have a low quality factor [11, 31] or that the air gap width d is smaller than assumed (see sections 3.4 and 4.3). Furthermore, the spectra show features that are shifted to lower frequencies compared to their theoretically predicted spectral positions (as indicated by the grey circles). This shift is, however, qualitatively consistent with the expected influence of the presence of the ZnSe on the band positions, as can be seen in Fig. 3.3.

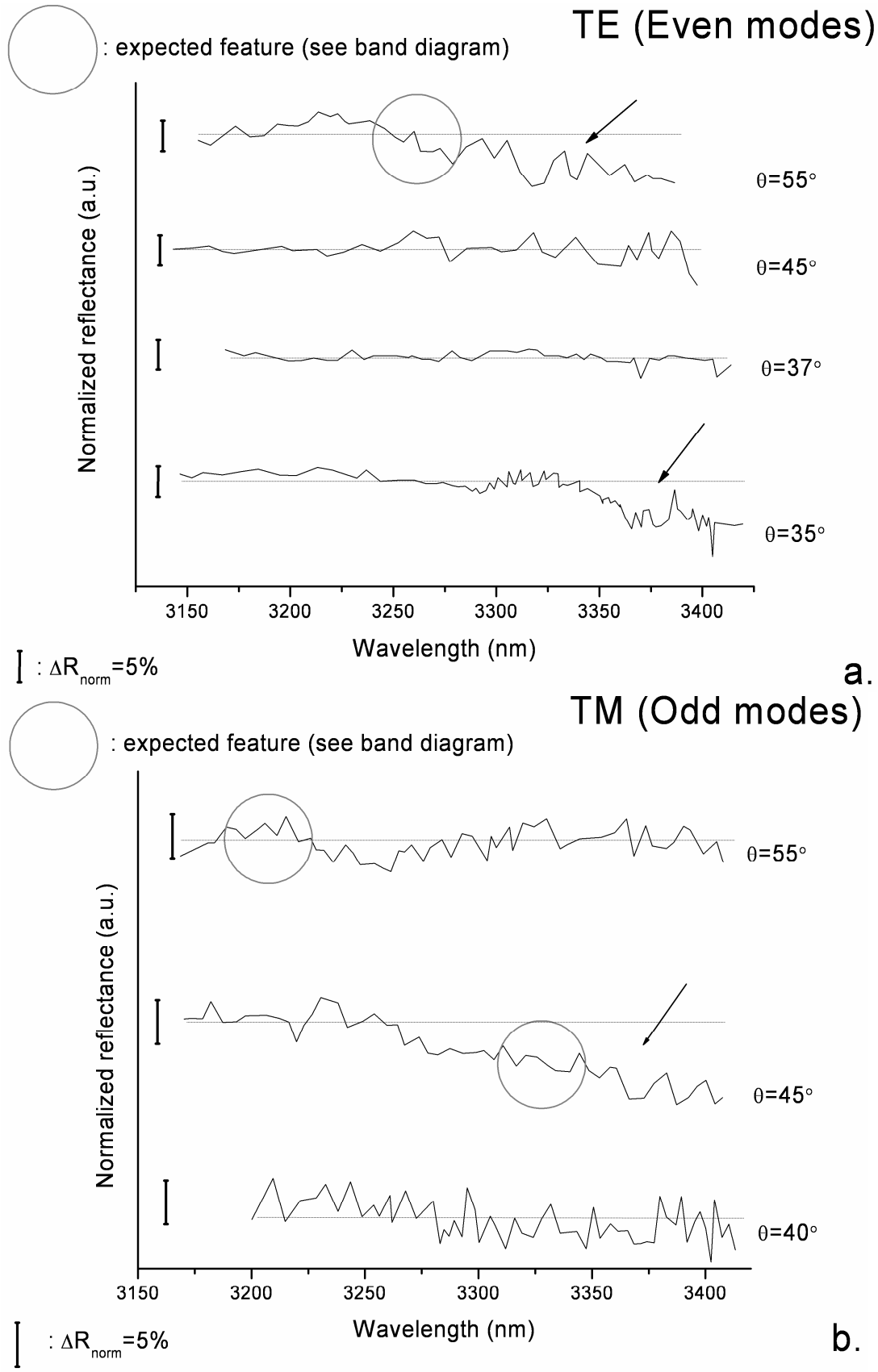

Figure 5.2: Measured ATR spectra, a) TE (top), b) TM (bottom)

6. Conclusions & recommendations

The optical properties of a 2D square-lattice PhC slab were theoretically examined. A theoretical band diagram was calculated using PhC parameters that were derived from earlier transmission and reflection measurements that probed the so-called leaky modes. In order to probe the guided modes of the sample, an ATR setup was designed and built. Spectral scans were performed covering a part of the MIR spectral region. These spectral scans show two features that can be attributed to theoretically expected resonances. These initial results demonstrate that this relatively simple setup can successfully couple to guided modes. However, the resonances that were measured are broader than expected and are only weakly visible compared to the background measurement noise. As the spectral broadening of measurements induced by the OPO mode hops (see section 4.4) and the angular spread of the beam (see sections 4.4 and 5.1) cannot account for this broadening, we must conclude that spectral broadening is the result of the vicinity of the ATR prism as well as irregularities in the PhC lattice. While it is possible that the bending deformation induced in the sample (see section 3.4) accounts for some broadening of the modes, we expect that this effect is small compared to other mode-broadening effects.

In order to accurately probe the position of guided modes as well as the lineshapes of associated resonances, it is required to decrease the magnitude of the broadening effects mentioned in the previous paragraph. This can be done by increasing the distance between the ATR hemisphere and the sample. By reducing all broadening effects that are induced by the setup rather than intrinsic bandwidth of the PhC's guided modes, this intrinsic bandwidth can be resolved. Increasing the coupling distance can be easily done using the distance control method described in section 3.4. As the exact band shapes are unknown, spectral features need to be tracked over several angles in order to obtain the minimum spectral width of a coupling resonance associated with a certain band. In the case of weak coupling (large coupling distance d) crystal irregularities are assumed to be the dominant factor affecting this minimum linewidth. It is of importance to obtain this spectral width, as it is related to the quality factor of a mode [10, 11, 12, 31], which gives a quantitative measure of the lifetime of a guided mode. This lifetime in turn is expected to influence the possible applications stated in chapter 1, such as enhanced $\chi^{(3)}$ effects through strong field confinement.

Furthermore, it is required to increase the signal-to-noise ratio (SNR) of the measurements, in order to accurately fit a Fano-type [10, 11, 31] lineshape to the measured features. This could be done by spectrally filtering the light incident on the detectors and by providing better shielding from external thermal noise sources. The integration time used for the measurements could be increased to 60 seconds rather than 30. It is recommended that lock-in amplification is used to filter background noise.

In order to obtain a full set of dispersion points to construct the guided mode band diagram, it is recommended that measurements are performed over a wider spectral range. Using the OPO used for the experiments described in this thesis, the sample could be examined in a spectral range ranging from 2.8-4 μm. As many bands are still expected to be present for smaller wavelengths (not shown in Fig. 2.9), it is

recommended that an additional light source is used to probe resonances corresponding to these bands. While modes at these wavelengths are of limited interest for potential applications involving third-order nonlinear optical effects (see chapter 1 and section 4.1), probing these modes would still provide a more complete characterization of the PhC.

It is also recommended that the PhC sample is examined over a large area using SEM to check for damages and irregularities, as these could account for mode broadening. The coupling mechanism could also be simulated using RCWA which would yield a theoretical ATR spectrum, which could be used to verify both the structure and coupling parameters. However, this cannot be done with the available RCWA software, as stated in chapter 4.

One improvement that could be made to the setup would be to mount fibers on rotation stages centered around the ATR prism's center, so that connecting the setup to an arbitrary light source and an arbitrary detector can easily be accomplished. This would make the coupling setup more compact and would also simplify alignment of the probe beam and the detector

The ATR coupling setup performed as expected while being relatively simple in design. The distance control scheme as described in section 3.4 allowed the coupling distance to be set with a high accuracy assuming the mechanical parameters of the sample under investigation are known. In many alternative ATR setups with complex distance control schemes, this is not the case and the coupling distance can only be determined from calculations fitted to measurements.

Acknowledgements

This thesis marks the end of my student life, which for me really means the end of an era. I've experienced a lot of ups and a few downs, and I'd like to thank a number of people for the role they played in the ups. First of all, I'd like to thank the people who have supervised my work in the Laser Physics group. These people include Prof. Klaus Boller, Dr. Petra Groß, and especially Dr. Peter van der Slot who was a great help during the final months of my research. Another special thanks goes out to the two people I've intensively worked with at this group, Ir. Ronald Hagen and Dr. Liviu Prodan. Ronald and Liviu, it's been a privilege (and fun) to work with you both.

A number of other people have provided invaluable input and experimental advice, without which I wouldn't have been able to finish the work described in this thesis. First of all, there is Dr. Feridun Ay of the IOMS group, the university's resident expert on evanescent field coupling. Ir. Dimitri Geskus of IOMS has provided me a nice SiON sample that I could use for the initial tests of my coupling setup (not described in this thesis). In our own group, Ing. Ab Nieuwenhuis, Dr. Chris Lee and Dr. Ian Lindsay have provided experimental help when I needed it. Thanks guys.

I'd also like to thank some additional people in and around the Laser Physics group for the measurable and statistically-significant effect they had on the atmosphere. So Peter, Bert, Ruud, Hein, Merel, Mark, Rolf, both Martijns, Leon, Olivier, Lars, Isabel, Balaji, Denny, Anton, Dennis, Jacob, Gerard, Arsen, Fred, Piet, Simone and Arie, as well as the resident lunch-sidekick-Nanochicks Verena and Saara-Maarit, thanks!

Outside of the university, two families have provided the social atmosphere I needed to keep me sane. The first is S.V. Arago, and especially the BACO and its (former) members. The other is the Famiglia di Bentrotti (and the Bentrotsch Brouw Genootschap), of the infamous Bentrotstraat student house. I'm not going to list all of them (because printing pages of names would be bad for the environment and I'd inevitably end up forgetting someone), except for one who is a member of both as well as my housemate and friend: Maarten, thanks.

Thanks as well to all of my other previously-unmentioned good friends (unaffiliated with aforementioned organizations), including (but not limited to) Naomi, Maarten, Maarten, Paul, Paul, Dirk, Daan, Chris, Joris, Vincent, Bart and Stan. People, please do something about the overlapping names in my circles of friends, as this could get confusing and really doesn't help me figure out whether I forgot anyone. If I did: sorry, I suggest you have your revenge by making my graduation party a costly affair.

And of course, special thanks go out to my parents and sister, who have been far more patient with me being a career-student than any parent should be.

Roel Arts, April 2008

References

[1] Yablonovich, E. (1989). *Inhibited Spontaneous Emission in Solid-State Physics and Electronics*. Phys. Rev. Lett. 58, pp. 2059-2062.

[2] Joannopoulos, J., Meade, R. & Winn, J. (1995). *Photonic Crystals: Molding the Flow of Light*. Princeton: Princeton University press.

[3] Yablonovich, E. & Gmitter, T.J. (1989). *Photonic band structure: The face-centered-cubic case*. Phys. Rev. Lett. 63, pp. 1950-1953.

[4] Haus, H.A. (1984). *Waves and fields in optoelectronics*. Prentice Hall.

[5] Locatelli, A. *et al.* (2004). *All-optical switching in ultrashort photonic crystal couplers.* Opt. Comm. 237 pp. 97-102.

[6] Jalali, B. (2008). *Can silicon change photonics?* Phys Status Solidi A 205, pp. 213-224.

[7] Maksymov, I.S., Marsal, L.F. & Pallares, J. (2006). *Modeling of two-photon absorption in nonlinear photonic crystal all-optical switch.* Opt. Comm. 269, pp. 137-141.

[8] Ibach, H. & Lüth, H. (2003). Solid-State Physics: An Introduction to Principles of Materials Science. Springer, 3rd ed. ISBN: 978-3540438700.

[9] Johnson, S. & Joannopoulos, J.D. (2001). *Block-iterative frequency-domain methods for Maxwell's equations in a planewave basis.* Opt. Express 8, pp. 173-190.

[10] Prodan L. *et al.* (2007). *Spectral investigation of a large-area 2D silicon photonic crystal slab for mid-IR radiation*. J. Phys. D Appl. Phys. 40, pp. 5571-5579.

[11] Hagen, R.A.J. (2007). *Spectral Investigation of a 2-Dimensional Photonic Crystal Slab for mid-Infrared Radiation.* MSc thesis, Laser Physics and Non-linear Optics, University of Twente.

[12] Prodan, L. *et al.* (2008). *Mid-infrared transmission of a large-area 2D silicon photonic crystal slab.* Accepted for publication in J. Phys. D Appl. Phys.

[13] Prodan L. *et al.* (2004). *Large-area two-dimensional photonic crystals for infrared light fabricated with laser interference lithography*. Nanotechnology 15, pp. 639-642.

[14] Ohtaka, K., Miyazaki, H. & Ueta, T. (1997). *Near-field effect involving photonic bands.* Mat. Sci. Eng. B-Solid 48, pp. 153-161.

[15] Dakss, M.L. *et al.* (1970). *Grating coupler for efficient excitation of optical guided waves in thin films.* Appl. Phys. Lett. 16, pp. 523-525.

[16] Muller, G., Abraham, K. & Schaldach, M. (1981). *Quantitative ATR spectroscopy: some basic considerations.* Appl. Opt. 20, pp. 1181-1190.

[17] Chung, P.S. (1974). *A graphical determination of the coupling efficiency by prism-film couplers in planar optical waveguides.* J. Phys. D Appl. Phys. 7, pp. 2490-2500.

[18] Galli, M. *et al.* (2005). *Measurement of Photonic Mode Dispersion and Linewidths in Silicon-on-Insulator Photonic Crystal Slabs.* IEEE J. Sel. Area. Comm. 23, pp. 1402-1410.

[19] Galli, M. *et al.* (2004). *Excitation of radiative and evanescent defect modes in linear photonic crystal waveguides.* Phys. Rev. B 70, 081307.

[20] Tien, P.K., Ulrich, R. & Martin, R.J. (1969). *Modes of propagating light waves in thin deposited semiconductor films.* Appl. Phys. Lett. 14, pp. 291-294.

[21] Seligson, J. (1987). *Prism couplers in guided-wave optics: design considerations.* Appl. Opt. 26, pp. 2609-2611.
[22] Galli, M. *et al.* (2005). *Single-mode versus multimode behavior in silicon photonic crystal waveguides measured by attenuated total reflectance.* Phys. Rev. B 72, 125322.
[23] COMSOL multiphysics, http://www.comsol.com
[24] Boyd, R.W. (2003). *Nonlinear Optics, second edition*. Academic Press.
[25] Haché, A. & Bourgeois, M. (2000). *Ultrafast all-optical switching in a silicon-based photonic crystal*. Appl. Phys. Lett. 77, pp. 4089-4091.
[26] Ling, Z.G. & Ajmera, P.K. (1987). *Lifetime measurements in semiconductors by infrared absorption due to pulsed optical excitation*. Appl. Phys. Lett. 51, pp. 1445-1447.
[27] Meisels, R. & Kuchar, F. (2007). *Density-of-states and wave propagation in two-dimensional photonic crystals with positional disorder.* J. Opt. A 9, S396-S402.
[28] Checoury, X. *et al.* (2005). *1.5 μm room-temperature emission of square-lattice photonic-crystal waveguide lasers with a single line defect*. Appl. Phys. Lett. 86, 151111.
[29] Soitec. Parc Technologique des Fontaines, 38190 Bernin, France
Website: http://www.soitec.com
[30] Fan, S. & Joannopoulos, J.D. (2002). *Analysis of guided resonances in photonic crystal slabs.* Phys. Rev. B 65, p. 235112.
[31] Prodan, L. (2008). *Mid-infrared characterization of two-dimensional photonic crystal slabs fabricated in silicon with laser interference lithography*. PhD thesis, ISBN: 978-90-365-2599-2.
[32] Lindsay, I.D. *et al.* (2006). *Mid-infrared wavelength- and frequency-modulation spectroscopy with a pump-modulated singly-resonant optical parametric oscillator.* Opt. Express 14, pp. 12341-12346.
[33] Harrick Scientific Products, Inc. 141 Tompkins Ave, 2nd floor. PO box 227. Pleasantville, NY 10570, USA. Website: http://www.harricksci.com
[34] Whittaker, D.M. & Culshaw, I.S. (1999). *Scattering-matrix treatment of patterned multilayer photonic structures.* Phys. Rev. B 60, pp. 2610-2618.
[35] Jundt, D.H. (1997). *Temperature-dependent Sellmeier equation for the index of refraction, n(e), in congruent lithium niobate*. Opt. Lett. 22, pp. 1553-1555.

Appendix: Posters & Publications

The following posters were presented concerning this project and can be seen on the next three pages:

B1. Arts, R. *et al.* (2008). *Guided-mode characterization of a 2D PhC through ATR*. Poster, Physics@FOM Veldhoven 2008.
B2. Prodan, L. *et al.* (2008). *Spectral investigation of a 2D photonic crystal slab for mid-IR radiation*. Poster, Physics@FOM Veldhoven 2008.
B3. Hagen, R. *et al.* (2007). *Two-color characterization of a 2D photonic crystal*. Poster, Physics@FOM Veldhoven 2007.

Contributions were made to the following publication: (copy not included in this appendix, but available on request)

Prodan, L. *et al.* (2008). *Mid-infrared transmission of a large-area 2D silicon photonic crystal slab.* Accepted for publication in J. Phys. D Appl. Phys.

Guided-mode characterization of a 2D PhC through ATR

R. Arts[a,c,*], L. Prodan[a,c], P.J.M. van der Slot [a,c], L. Kuipers[b,c,d] and K.-J. Boller[a,c]

a. Laser Physics and Nonlinear Optics group, Department of Science & Technology, University of Twente

b. Optical Sciences, Department of Science & Technology, University of Twente

c. MESA+ research institute, University of Twente

d. Center for Nanophotonics, FOM-Institute for Atomic and Molecular Physics (AMOLF)

**R.Arts@student.utwente.nl*

Introduction

A 2D square-lattice SOI photonic crystal (PhC) slab for providing mid-IR photonic resonances (Fig. 2) was fabricated using Laser Interference Lithography (LIL) [1]. The leaky modes of this sample were previously characterized by specular reflection [2] and transmission. In order to also characterize the guided modes of this slab, a setup was built for evanescent-field coupling to the PhC slab's modes (Fig. 1).

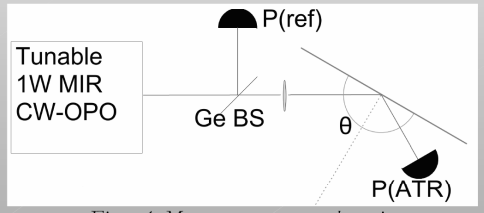

Figure 1: Measurement setup - schematic

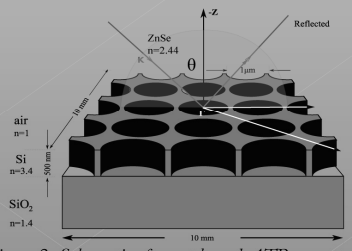

Figure 2: Schematic of sample and ATR - not to scale

Experimental aspects

- **Attenuated Total Reflection (ATR) setup to measure coupling**
- **Two critical parameters: coupling distance D (Fig. 3) and phase matching angle θ (Fig. 2)**
- **High-index (ZnSe) hemisphere for wide range of accessible k-vectors (Fig. 2)**
- **CW-OPO MIR source with Watt-level power, high spectral resolution and single spatial mode [3].**
- **Coupling distance D controlled by pressure on one end, Ni foil on the other end (Fig. 3)**
- **Deformation calculated - Comsol Multiphysics (Fig. 4)**

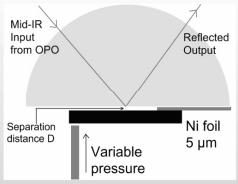

Figure 3: Experimental setup with control of the coupling distance

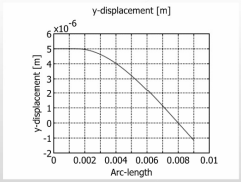

Figure 4: Deformation of sample (Comsol)

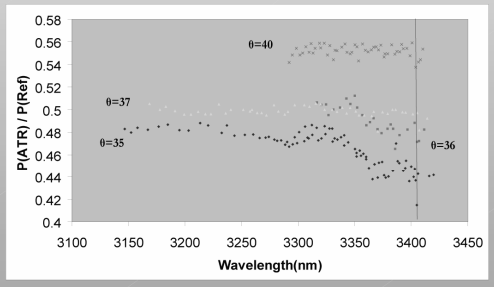

Figure 5: Mid-infrared reflectivity spectra

Results

Measured reflectivity spectra, normalized to reference measurements (Fig. 1), are shown for four different angles of incidence (Fig. 5). These measurements show a resonance near 3.4 microns (vertical line). This resonance appears to be dispersion-free, i.e. doesn't shift much with angle, which is consistent with theoretical calculations [2]. Further experimental investigations will be done. The origin of the resonance feature between 3.35 and 3.4 microns for θ=35 has yet to be determined. After a successful evanescent coupling into guided modes, ultrashort (mid-IR) pulses in increased intensity could be launched into the crystal to study nonlinear (Kerr-type) of effects.

Additionally, we are considering to excite guided modes using electron beams [4]. This is of interest for so-called photonic FELs [5].

[1] Prodan, L. et al (2004). *Large-area two-dimensional silicon photonic crystals for infrared light fabricated with laser interference lithography* . Nanotechnology 15, pp. 639-642

[2] Prodan, L. et al (2007). *Spectral investigation of a large-area 2D silicon photonic crystal slab for mid-IR radiation* . J PHYS D APPL PHYS 40 (18), pp. 5571-5579

[3] Lindsay, I.D. et al (2006). *Mid-infrared wavelength- and frequency-modulation spectroscopy with a pump-modulated singly-resonant optical parametric oscillator.* OPT EXPRESS 14, pp. 12341-12346

[4] C. Luo et al (2003). *Cerenkov Radiation in Photonic Crystals.* Science 299, pp. 368-371.

[5] http://www.stw.nl - project number 08128

FOM MESA+ Institute for Nanotechnology University of Twente Enschede - The Netherlands

Spectral investigation of a 2D photonic crystal slab for mid-IR radiation

L. Prodan,[a,b] R. Hagen,[a] R. Arts,[a] P. Gross,[c] L. Kuipers[d,e] and K-J Boller[a]

a. Laser Physics and nonlinear Optics group, Department of Science & Technology, University of Twente
b. Laser Applicatie Centrum, University of Twente
c. Optical Technologies Group, University of Münster
d. Optical Sciences, Department of Science & Technology, and MESA Research Institute, University of Twente
e. Center for Nanophotonics, FOM-Institute for Atomic and Molecular Physics (AMOLF)

Goal of the Project: We investigate the transmission of large area, 1 x 1 cm^2 photonic crystal, fabricated by Laser Interference Lithography (LIL). The transmission was recorded over a broad wavelength range from 1.1 to 2.4 μm, i.e., from the near-infrared single photon absorption edge of silicon to below the mid-infrared two-photon absorption edge. The transmission measurements through a photonic crystal at such scale are of high interest for practical applications of light filtering.

Photonic Crystals (PhC): are composites materials, for which a large, periodic variation of the dielectric function leads to a dramatic change of the propagation properties of light.

The sample is fabricated using Laser Interference Lithography (LIL) [1]. The basis is a 0.5mm thick silicon substrate, covered with a 3000nm silicon oxide buffer layer, and with a 500nm thin silicon layer on top. The silicon top layer carries the photonic structure, namely round air holes with 760nm diameter in a square pattern with 1000nm perioidicity. The holes cover a very large area of 1 x 1 cm^2.

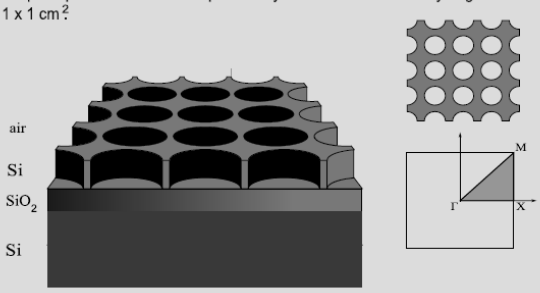

Method of Investigation: The transmission spectra are measured under normal incidence using a Cary 5E spectrometer. Spectra are recorded using linearly polarized light, with the E-field aligned along the crystal symmetry directions, as well as for light polarized perpendicularly.

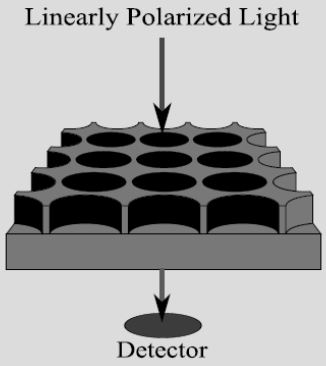

Results:

Measurements for one crystal symmetry direction, carried out with different polarizations, yield identical traces. From this polarization independence it follows, that the holes are round and that the photonic crystal shows true four-fold rotation symmetry.

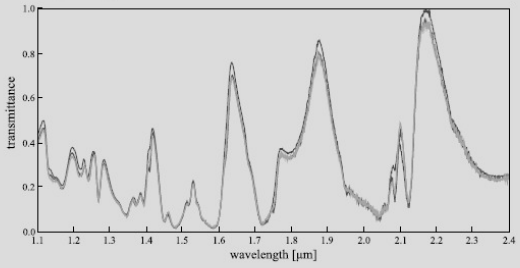

Transmission of polarized light through the photonic crystal, with E-field aligned along the ΓX (red trace, crystal rotation 0°), along an intermediate direction (green trace, 22.5°), and along ΓM direction (orange trace, 45°).

Results:

Comparison of measurements with theoretical predictions

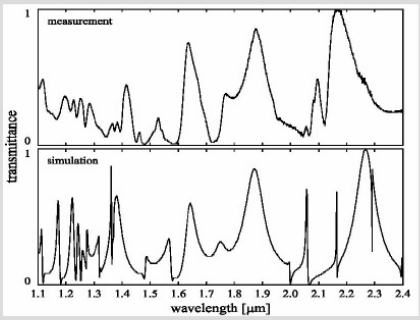

The spectra show narrow-bandwidth Fano-type resonances superimposed onto a broader Fabry-Perot-type background. Calculated spectra generated using coupled-wave analysis show agreement in width, height and position of the resonances.

Fano fit [2] to determine the quality factor Q

$$\mathrm{Fano}(f) = 1 + \frac{q^2 - 1 + \frac{4q(f - f_0)}{\gamma}}{1 + \left(\frac{2(f - f_0)}{\gamma}\right)^2}$$

coupling parameter q
frequency f
center frequency f_0
fwhm γ

$$Q = \frac{f_0}{\gamma}$$

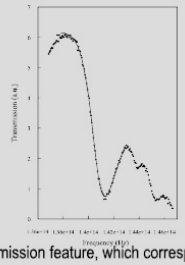

The fit function yields the bandwidth of each transmission feature, which corresponds to the life time of a photonic crystal resonance. From these, we derive an average quality factor Q of around 50. For an ideal photonic crystal, quality factors of 300 are expected. The reduction can be attributed to imperfections of the manufacturing process (mainly side wall roughness due to the etching).

Conclusions

- This work provides the first experimental demonstration in transmission of Fano-type resonances in 2D silicon photonic crystal slabs at mid-infrared wavelengths.
- Being able to operate in this spectral range is of importance to allow later investigations on nonlinear optical switching of the crystal transmission with reduced losses through two-photon absorption.
- Narrow transmission resonances demonstrate suitability of PhC slabs for practical filter applications.
- The agreement between experiment and theory demonstrate that the coupled-wave analysis method can be used to determine the transmission of the slab under normal incidence.

References

[1] L. Prodan, T.G. Euser, H.A.G.M. van Wolferen, C. Bostan, R.M. de Ridder, R. Beigang, K-J Boller and L. Kuipers, Nanotechnology 15, 639 (2004)
[2] U. Fano, Phys. Rev. 124, 1866 (1961).

Two-color characterization of a 2D photonic crystal

R. Hagen[a], R. Arts[a], L. Prodan[a], P. Gross[a], L. Kuipers[b,c] and K-J Boller[a]

a. Laser Physics and nonlinear Optics group, Department of Science & Technology, University of Twente
b. Optical Techniques Group, Department of Science & Technology, and MESA+ Research Institute, University of Twente
c. Center for Nanophotonics, FOM-Institute for Atomic and Molecular Physics (AMOLF)

University of Twente
Enschede - The Netherlands

Goal of the Project: As preparation for studies of the nonlinear properties of a photonic crystal (PhC), we have carried out a linear reflectivity characterization in the MIR range around 2.5 μm and, also, in the range of half of those wavelengths (around 1.25 μm). The latter, and comparison with the theoretically expected band structure, should provide additional information on the optical properties of the fabricated crystals.

Photonic Crystal: Schematic drawing of a 2D PhC. The sample is fabricated with Laser Interference Lithography (LIL) to create a large area crystal[1].

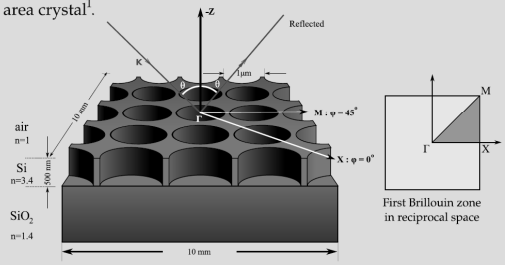

Method of Investigation[2]: Measure the reflectivity as a function of wavelength along the two symmetry directions ΓX and ΓM for a range of incident angles θ. Information on the mode structure can be obtained from Fano-like features[3] in the reflectivity spectra.

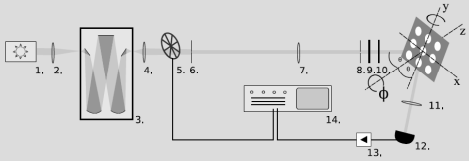

1. White light source
2. Lens
3. Monochromator
4. Lens
5. Optical chopper
6. Diaphragm
7. Lens
8. Diaphragm
9. Filter
10. Polarizer
11. Lens
12. Detector
13. Amplifier
14. Lock-in amplifier

Reflectivity spectra along ΓX direction

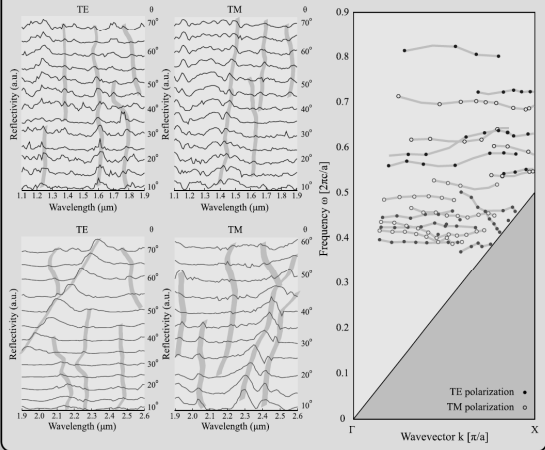

Reflectivity spectra along ΓM direction

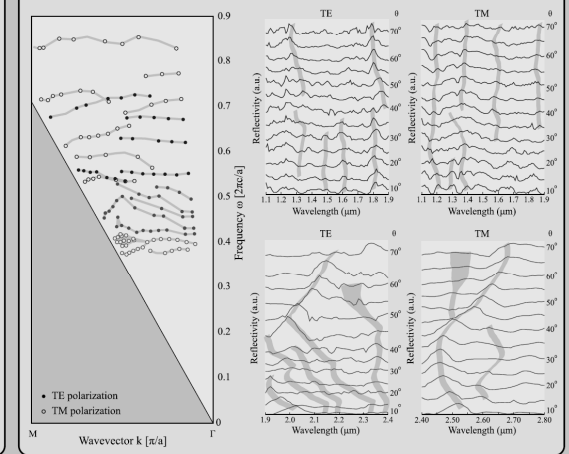

Quality factor distribution for ΓX

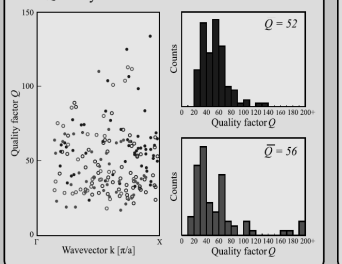

Fano fit to determine the quality factor Q

The lifetime of a PhC mode is related to the Q-factor of the photonic crystal

$$\mathrm{Fano}(f) = 1 + \frac{q^2 - 1 + \frac{4q(f - f_0)}{\gamma}}{1 + \left(\frac{2(f - f_0)}{\gamma}\right)^2}$$

coupling parameter q
frequency f
center frequency f_0
fwhm γ

$$Q = \frac{f_0}{\gamma}$$

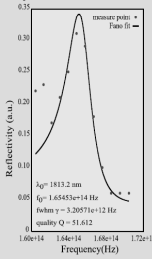

Quality factor distribution for ΓM

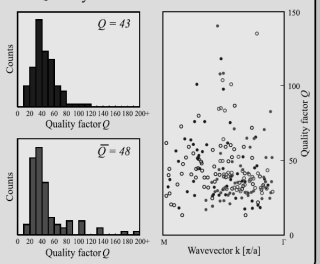

Conclusions

The Q-factor for a 2D photonic crystal is determined from resonance features in reflectivity spectra measured with two colors.

The experiments yield an average Q-factor of 50 with a deviation of 29.

References

[1] L. Prodan, T.G. Euser, H.A.G.M. van Wolferen, C. Bostan, R.M. de Ridder, R. Beigang, K-J Boller and L. Kuipers, Nanotechnology 15, 639 (2004)
[2] V. N. Astratov, I. S. Culshaw, R. M.Stevenson, D. M.Whittaker, M. S. Skolnick, T. F. Krauss, and R. M. De La Rue, J. Lightwave Techn. 17, 2050 (1999)
[3] U. Fano, Phys. Rev. 124, 1866 (1961).